MATERIALS PROCESSING HANDBOOK

EDITED BY
JOANNA R. GROZA
JAMES F. SHACKELFORD
ENRIQUE J. LAVERNIA
MICHAEL T. POWERS

CRC Press
Taylor & Francis Group
Boca Raton London New York

CRC Press is an imprint of the
Taylor & Francis Group, an informa business

Cover: Si nano-bridges between two vertical Si walls synthesized using metal-catalyzed chemical vapor deposition. The work was done at Quantum Science Research group of Hewlett Packard Laboratories. -M. Saif Islam, University of California, Davis, CA

CRC Press
Taylor & Francis Group
6000 Broken Sound Parkway NW, Suite 300
Boca Raton, FL 33487-2742

Printed in the United States of America on acid-free paper
10 9 8 7 6 5 4 3 2 1

International Standard Book Number-10: 0-8493-3216-8 (Hardcover)
International Standard Book Number-13: 978-0-8493-3216-6 (Hardcover)

Library of Congress Cataloging-in-Publication Data

Materials processing handbook / editors: Joanna R. Groza ... [et al.].
p. cm.
Includes bibliographical references and index.
ISBN-13: 978-0-8493-3216-6 (0-8493-3216-8 : alk. paper)
1. Manufacturing processes--Handbooks, manuals, etc. 2. Materials science--Handbooks, manuals, etc. I. Groza, Joanna R.

TS183.M3827 2007
670--dc22 2006030545

Visit the Taylor & Francis Web site at
http://www.taylorandfrancis.com

and the CRC Press Web site at
http://www.crcpress.com

17

Rapid Solidification and Bulk Metallic Glasses — Processing and Properties

Jörg F. Löffler,
Andreas A. Kündig, and
Florian H. Dalla Torre
Laboratory of Metal Physics and Technology, ETH Zurich

List of Symbols

a	Notch length
A_v	Constant
B	Bulk Modulus
Δc_p^{l-x}	Molar heat capacity difference between liquid and crystal at constant pressure
$c_p\rho$	Heat capacity per unit volume at constant pressure
$\bar{c}$	Correction factor of $\sim$1.1
D	Atomic diffusivity
D^*	Fragility parameter
d	Dimension
d_c	Critical casting thickness
$D_e = \dot{\gamma}\tau$	Deborah number
E	Young's modulus
f	Crystalline volume fraction
$f(Q)$	Atomic scattering factor
G	Shear modulus
G'	Storage modulus
G''	Loss modulus
G_c	Critical strain energy release rate, with c the critical point at fracture
ΔG^*	Energy barrier for forming of a nucleus
ΔG_v	Gibbs free energy difference (liquid to crystal) per unit volume
ΔH_m^f	Molar enthalpy of fusion
$I(Q)$	Normalized elastic scattering intensity
I_v	Nucleation rate (per volume)
j_Q	Endothermic heat flow
k_B	Boltzmann constant
$K_c = \sqrt{EG_c}$	Fracture toughness, with c the crucial point at fracture
l	Atomic diameter
N_A	Avogadro's constant
$\mathbf{Q}$	Scattering vector
R	Gas constant
r	Distance (from a central atom)
r^*	Critical radius of a nucleus
R_c	Critical cooling rate
$S(Q)$	Atom–atom interference function
ΔS	Normalized thermal stability
ΔS_m^f	Molar entropy of fusion
$\Delta T = T_x - T_g$	Undercooled liquid regime
t	Crystallization time
T_0	Vogel–Fulcher–Tammann temperature
T_{r0}	Reduced Vogel–Fulcher–Tammann temperature
T_g	Glass transition temperature
T_{liq}	Liquidus temperature
T_r	Reduced temperature
$\Delta T_r = 1 - T/T_{liq}$	Relative undercooling
T_{rg}	Reduced glass transition temperature
T_x	Crystallization temperature
v	Growth velocity
V_m	Molar volume
$\alpha = \kappa/(c_p\rho)$	Thermal diffusivity
$\tilde{\alpha} \equiv \dfrac{(N_A V_m^2)^{1/3}\gamma}{\zeta(T)\Delta H_m^f}$	Constant

$\tilde{\beta} \equiv \dfrac{\zeta(T)\Delta S_{\mathrm{m}}^{\mathrm{f}}}{R}$	Constant
γ	Interfacial energy (per unit area)
$\dot{\gamma}$	Shear strain rate
ε	Strain
$\dot{\varepsilon}$	Strain rate
$\zeta(T)$	Temperature-dependent correction factor
η	Viscosity
$\tilde{\eta}$	Constant inversely proportional to the molar volume of the liquid
η^*	Complex viscosity (from dynamic measurements)
η_0	Viscosity extrapolated to shear strain rate $\dot{\gamma} = 0$
θ	Diffraction angle
κ	Thermal conductivity
λ	X-ray wavelength
ν	Poisson's ratio
ρ_0	Average atomic number density
$\rho(r)$	Pair distribution function
σ	Flow stress
σ_{y}	Yield strength
τ	Relaxation time
τ_{c}	Characteristic cooling time
τ_{s}	Shear stress
ω	Angular frequency

Abstract

This chapter describes various processing techniques for the preparation of metastable phases, with a focus on metallic glasses. Following a general introduction, Section 17.1 outlines various methods of amorphization and rapid solidification. Special attention is given to *bulk* metallic glasses, a new class of alloys that can be manufactured as massive amorphous pieces in dimensions of several centimeters at cooling rates less than 100 K/s. Section 17.2 describes the microstructure of metallic glasses and highlights the most relevant atomic models, while Section 17.3 relates the thermophysical properties of metallic glass-forming liquids with their glass-forming ability. A time–temperature–transformation diagram of undercooled liquids is derived theoretically and compared with experimental data to provide the basis for Section 17.4, in which the processing of metallic glass-forming melts is described. There, methods of injection casting and superplastic forming of undercooled liquids that can be applied to today's bulk metallic glass-formers are discussed; also presented are a concept and preliminary experimental results on the co-extrusion of metals and polymers to obtain a new form of metal/polymer composites. Section 17.5 outlines mechanical properties at elevated and ambient temperatures, and discusses homogeneous and inhomogeneous deformation in metallic glasses. This topic is extended in Section 17.6, where the synthesis and processing of bulk metallic glass composites and their potential use as structural material are presented. The chapter concludes with Section 17.7, which highlights the various applications of (bulk) metallic glasses.

17.1 Introduction

17.1.1 General Terms

Rapid quenching of metals in water has been a familiar process for about two millennia, ever since the first blacksmiths began making tools and weapons from steel and other alloys strengthened by solid-solution or work hardening. Nowadays rapid quenching is still a major technique in materials manufacturing, and cooling rates depend greatly on the size of the component and the techniques used.

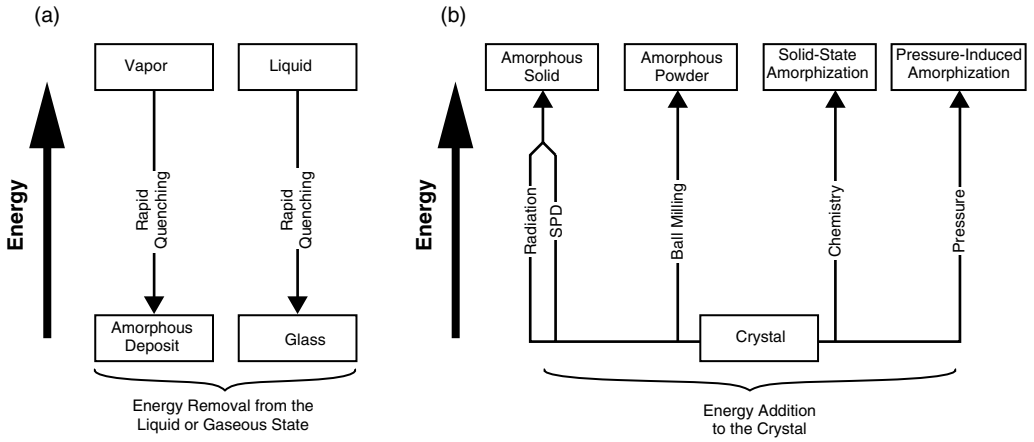

FIGURE 17.1 Schematic diagrams representing the various amorphization techniques, where (a) energy is extracted from a vapor or liquid phase, or (b) where energy has to be added to the system. Note that the term "glass" is restricted to an amorphous material created via cooling from the liquid state (SPD stands for severe plastic deformation).

As illustrated in Figure 17.1, amorphization techniques are basically divided into those methods where energy (heat) has to be rapidly extracted from the gaseous or liquid state[1–12] (Figure 17.1a), or where energy has to be added to the solid system (crystal)[5,7,13–17](Figure 17.1b). In the latter case, energy is provided to the crystal in the form of chemical reactions (solid-state amorphization[13]), radiation (amorphization by high-energy neutrons, protons, heavy ions or electrons[14] — see also Chapter 10), pressure (pressure-induced amorphization[15]), deformation and cold welding (mechanical milling[16]), or shear (severe plastic deformation[17]). More details about pressure and deformation effects are given in Chapter 13.

For historical reasons, only amorphous materials produced via rapid quenching from the liquid state are called *glass*. This does not apply to amorphous materials produced by techniques unrelated to quenching (Figure 17.1b). In this article, we have restricted ourselves to rapid solidification techniques from the liquid (and more rarely from the gaseous) state. For the amorphization techniques unrelated to quenching the reader is referred to References 13–17.

The first metallic glass (an eutectic Au–Si alloy[2]) was discovered in 1960 by P. Duwez and coworkers at CalTech, Pasadena. This discovery occurred by chance: the actual aim of the research project was to produce nonequilibrium solid solutions to verify whether the Hume–Rothery rule applies to solid solutions based on copper and noble metals.[18,19] Duwez successfully managed to quench Cu–Ag and Ag–Ge alloys[3] into a single phase, which showed that solid solubility can indeed be increased by rapid solidification from the melt, as shown earlier for vapor quenching.[1] Duwez's technique is still used today to produce metastable crystalline phases, as metastable phase formation can improve various properties as compared to the equilibrium crystalline state. Rapid solidification of crystalline alloys shows, for example, improved mechanical strength due to enhanced solid solubility and reduced grain size.[20] Examples for the formation of metastable phases upon rapid solidification are given in Reference 7.

The glassy Au–Si alloy discovered by Duwez was produced in dimensions of less than 50 μm, which is why a very high cooling rate of approximately 10^6 K/s resulted. Sample dimension and cooling rate are in fact closely related in rapid melt solidification. The lowest cooling rate required to produce a glassy material from the melt is termed "critical cooling rate," R_c. The maximum thickness at which a material can be produced glassy is termed "critical casting thickness," d_c. As heat must be extracted from the melt, the critical casting thickness can be calculated from the Fourier heat flow equation, $\partial T/\partial t = \alpha \nabla^2 T$, where $\alpha = \kappa/(c_p \rho)$ is the thermal diffusivity, κ is the thermal conductivity and $c_p \rho$ is the heat capacity per unit volume at constant pressure. The solution to this equation with the corresponding boundary conditions involves a characteristic cooling time, $\tau_c = d^2/\alpha$, required by a molten sample of typical dimension

d and initial temperature T_{liq} (liquidus temperature of the alloy) to achieve ambient temperature. The asymptotic cooling rate $\partial T/\partial t$ is then

$$\dot{T} = \frac{T_{liq}}{\tau_c} = \frac{\alpha T_{liq}}{d^2} = \frac{\kappa T_{liq}}{c_p \rho d^2}. \tag{17.1}$$

With typical values for a metallic melt [$\kappa \approx 4$ W/(m K), $c_p\rho \approx 2$ J/(cm^3 K), and $T_{liq} \approx 1000$ K], one obtains

$$\dot{T}(\mathrm{K/s}) \approx \frac{20}{d^2(\mathrm{cm}^2)}. \tag{17.2}$$

Thus, a sample of 50 μm thickness can be cooled at a rate of approximately 10^6 K/s, or, in other words, a liquid alloy needs to be cooled at a rate of 10^6 K/s to produce a glassy alloy with a critical casting thickness of $d_c = 50$ μm, while an alloy with critical cooling rate $R_c = 20$ K/s can be produced with a dimension of 1 cm.

Ever since the discovery of the first metallic glass, researchers have tried to improve glass-forming ability, the latter being synonymous with a reduction in the critical cooling rate or an increase in the critical casting thickness. In fact, a few years after Duwez's discovery, Chen and Turnbull were able to make glassy spheres of ternary Pd–Si–N with N = Ag, Cu, or Au,[21] and the alloy $Pd_{77.5}Cu_6Si_{16.5}$ could be quenched into a glass with a diameter of 0.5 mm. This alloy also showed a distinct glass transition, which motivated the Turnbull group to extend the general theories of the glass transition[22,23] to metallic glasses.[24,25] As outlined in more detail in Section 17.2, it was found that alloys with good glass-forming ability generally show a high "reduced glass transition temperature" T_{rg} ($\sim$2/3), which is defined as

$$T_{rg} = \frac{T_g}{T_{liq}}, \tag{17.3}$$

where T_g is the glass transition temperature and T_{liq} the liquidus temperature of the alloy.

Parallel to the discoveries of the first metallic glasses and the scientific interest they attracted, various production techniques were developed, such as gun quenching, splat quenching, or melt spinning, which facilitated the application of high cooling rates to metallic liquids (see details in Section 17.1.2). A strong interest in up-scaling emerged in the 1970s, when Fe-based metallic glasses with improved soft-magnetic properties were discovered (for an overview, see e.g. Reference 26). This led to the development of the planar flow casting technique (e.g. Reference 27), where amorphous ribbons of a few tens of microns in thickness, a few tens of centimeters wide, and several meters long could be produced and successfully implanted into transformer cores.

Further development and refinement of synthesis methods for ternary metallic glass systems (Pd–Cu–Si[28], Au–Pb–Sb[29], Pd–Ni–P[30,31]) showed the potential for metallic glasses to be produced in sample dimensions more closely representing a bulk material. However, such bulk metallic glasses were long regarded as laboratory curiosities and as nonreproducible on a larger scale. This situation changed in the 1990s when more complex quaternary and quinary metallic glasses, showing critical cooling rates of less than 100 K/s, were developed by the groups of Inoue (Tohoku University, Sendai, Japan)[32–34] and Johnson (CalTech, Pasadena).[35–37] These findings in turn motivated the development of liquid metal quenching methods, which enabled the casting of massive samples in a controlled manner and led to the first bulk metallic glasses.

Figure 17.2 shows various metallic glass-forming alloys plotted according to their critical cooling rate (and associated critical casting thickness) as a function of their reduced glass transition temperature (see also Reference 38). The rapid solidification techniques (discussed in more detail in Section 17.1.2) are also correlated with the quenching rate. The highest possible quenching rate needed for an elemental face-centered cubic (fcc) metal to amorphize cannot be reached experimentally, but has been achieved in computer simulations.[39,40] The highest experimental cooling rate has so far been attained using laser quenching (R_c estimated in Reference 38). However, this technique is restricted to small droplets corresponding to

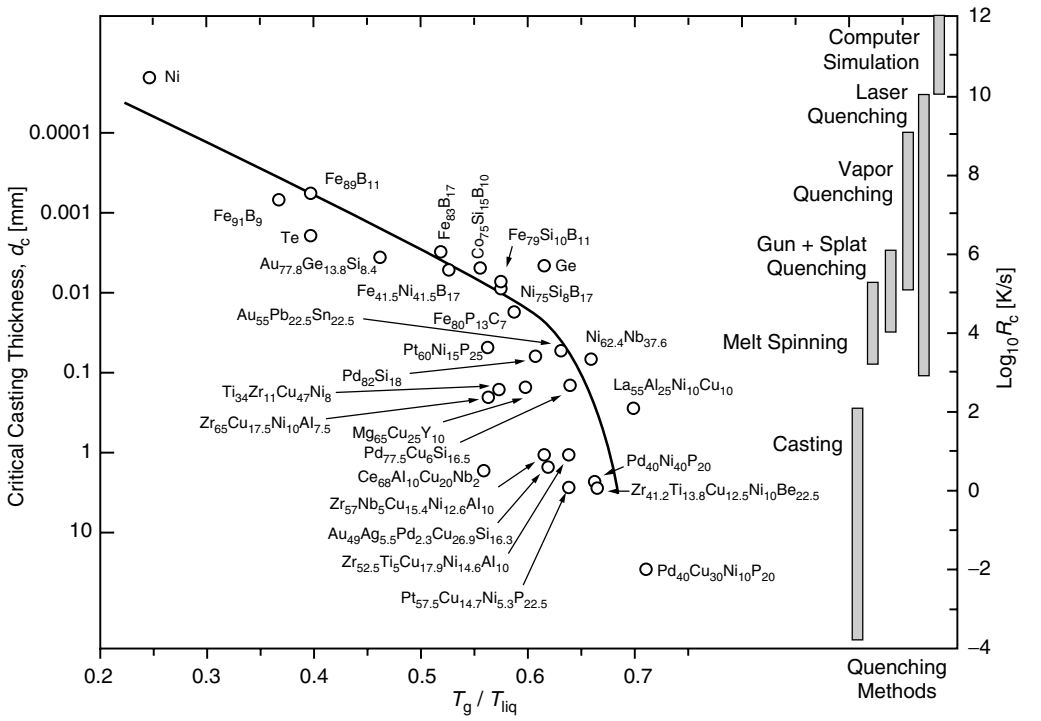

FIGURE 17.2 Critical casting thickness, d_c, and critical cooling rate, R_c, vs. reduced glass transition temperature T_g/T_{liq} for various metallic glass-forming alloys and correlated with the various quenching techniques.

the spot size of the high-intensity laser beam, and is thus not discussed further. In Section 17.1.2 the other techniques shown in Figure 17.2 are presented in the descending order of their achievable cooling rates.

17.1.2 Rapid Quenching Techniques

17.1.2.1 Vapor Quenching

Vapor quenching, or gas condensation, was initially used for research purposes and goes back to the work of Kramer,[41] and of Buckel and Hilsch.[1] They deposited metal films from an evaporation source onto a liquid-helium-cooled substrate, which led to increased solid solubility or, in a few cases, to amorphization of the metal film. Later work has concentrated on processes to increase the dimensions of possible products either by sputtering[42] or vapor quenching.[43]

With the investigation of nanocrystalline metals instigated by the work of Gleiter and coworkers,[44,45] vapor quenching via an inert-gas condensation technique (IGC) or via sputtering has now re-emerged in the research community. The goal of this ongoing research field is to study the size effects of mechanical, structural, and other physical properties in elemental metals and alloys. In contrast to the other methods mentioned above, in IGC the metal solidifies first as a powder and is then compacted to solid samples in a second step. Figure 17.3 shows a schematic drawing of an IGC facility. The system is divided into four parts: a loading unit (A), a main ultrahigh vacuum chamber (B), a compression unit (C), and a special charging device (D) to potentially press powders prepared by other techniques. The material is thermally evaporated from a resistive heating device (e.g., a tungsten boat [E]) into a 10^{-6} Pa base pressure vacuum system filled with 100 Pa of 99.999% pure He gas (B). During the IGC process (F) the atoms in the vapor phase condense to form small nanometer-sized crystallites that are collected on a rotating cylinder (G) cooled by liquid nitrogen. The powder is scraped off (H) into a funnel (I) and transferred to the compaction unit (C). After re-evacuation to the initial pressure of 10^{-6} Pa the powder is consolidated by pressing

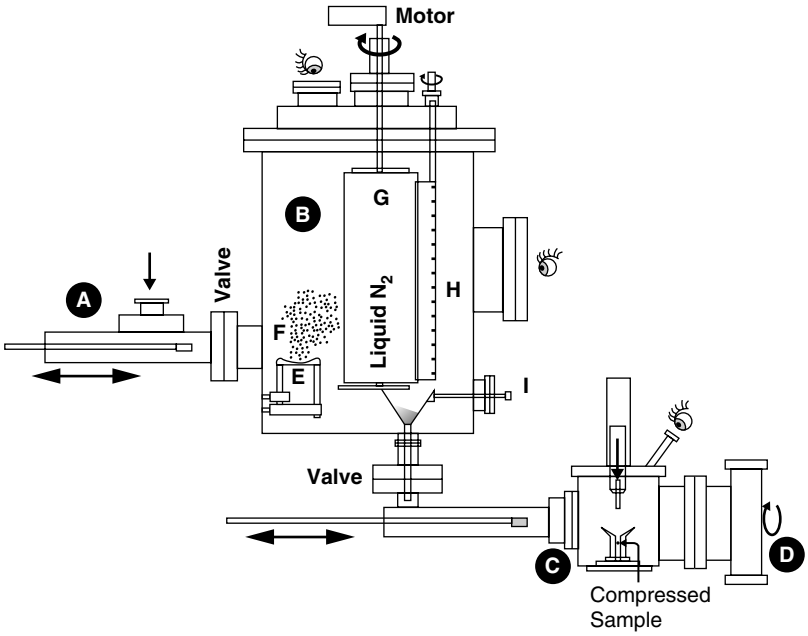

FIGURE 17.3 Schematic drawing of an inert-gas condensation facility to produce nanocrystalline metallic alloys by vapor quenching and consolidation.

(1 to 2 GPa) at room temperature or elevated temperatures. This technique allows bulk nanocrystalline materials to be produced with typical dimensions of 1 cm diameter and 1 mm height and crystal sizes of approximately 10 nm. Research into these nanocrystalline materials has contributed significantly to an understanding of the influence of small crystallites on physical properties, as compared to that of their coarse-grained counterparts.[46]

17.1.2.2 Gun and Splat Quenching, Melt Spinning

The first glassy alloys were prepared using a so-called "gun quenching" technique. With this technique, invented by Duwez and coworkers, it was possible to achieve cooling rates of $\sim 10^6$ Kelvin per second. A detailed description is given in Reference 47. The gun quenching technique led to the development of an apparatus capable of producing larger sample dimensions. The so-called "splat quencher" or "drop smasher," shown in Figure 17.4a, enables the production of discs of approximately 1 to 4 cm in diameter with thicknesses of up to 50 μm. A small mass is levitated in an induction coil using a high frequency current and melted. The current is then switched off; the molten droplet falls and triggers, via a laser signal, two pneumatically or electromagnetically driven flat pistons that collide at high speed and quench and flatten the molten drop to a "splat" (a thin foil) at a cooling rate of $\sim 10^6$ K/s. The configuration used today is adapted from that shown in Figure 17.4a.

Further studies of metallic glasses have increased the complexity of systems and the number of constituent elements, leading to a decrease in the critical cooling rate (Figure 17.2). Once the potential of metallic glasses for various applications (in particular in their promising soft-magnetic properties) was recognized, it was seen that a scaling-up method was needed to deploy metallic glasses commercially. In the 1970s several researchers developed continuous casting or melt spinning methods in response to this requirement.[27,48,49] These techniques facilitated the production of metallic ribbons cast onto a rotating copper wheel, as is shown schematically in Figure 17.4b. Further improvements and variations of the melt spinning apparatus resulted in glassy metal ribbons of several meters in length and a few centimeters in width, using either a single wheel or a twin-roller configuration where the melt is quenched in between (see also Reference 47). In principle there are two main differences in how the metal is fed onto the rotating

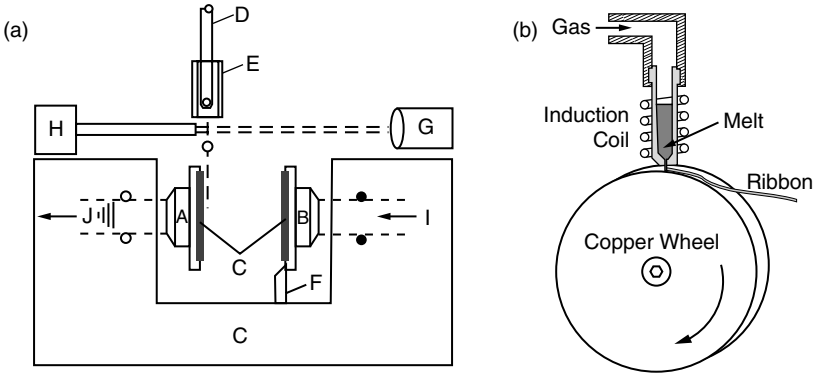

FIGURE 17.4 Schematic drawing of (a) splat quencher and (b) melt spinner. (17.4a from Johnson, W.L., *Metals Handbook* 2, 805, 1990. With permission.)

substrate. In chill-block melt spinning the liquid is pressed with an inert gas from the nozzle, from which a liquid stream of metal drops onto the spinning copper wheel (see Figure 17.4b).[50] In pendant-drop melt extraction all of the solid metal is fed from above and heated inductively just above the spinning wheel, where the molten phase is continuously dragged away by the rotor.[51] This method also makes possible the production of wires using a knife edge on the copper wheel.

In planar flow casting, an advanced version of the classical chill-block melt spinning, a narrow, precise distance between the nozzle and the copper wheel is maintained to constrain the melt between the wheel and the nozzle and generate a stable melt flow. Using this process it is possible to use rectangular nozzles of several tens of centimeters in width and manufacture large amorphous metal sheets.[52] This method has been applied commercially since the 1970s in the production of soft-magnetic ferrous foils for use in transformer cores (see also Section 17.7.1). A detailed description of this and other rapid quenching techniques can be found in Reference 53.

17.1.2.3 Copper Mold Casting and Injection Casting

In the early 1990s, the development of complex multicomponent metallic glasses[32–37] with very low critical cooling rates (even down to 1 K/s[35]) provided a new and so far uninterrupted scientific and commercial impetus to the search for new bulk metallic glasses and research into their physical properties and possible applications. It is now possible to quench bulk metallic glass samples in large copper molds with either inductive (radio frequency, RF) or inert-gas plasma arc heating. There are two basic techniques for forcing the liquid into a mold: either (1) the use of an inert-gas pressure difference (via inert-gas pressure injection or suction casting), or (2) piston injection, where a solid piston shoots the melt into a copper mold. These systems have so far mainly been used in configurations similar to that of Figure 17.5, where the material is kept in either a quartz or boron-nitride crucible during heating, before being cast into the mold via application of a pressure difference. Various versions of the setup shown have also been built to create the special conditions required for the successful casting of metals such as Ca-based or Mg-based bulk metallic glasses that are reactive and have a low vapor pressure. For more information on the varieties of copper mold casting techniques, the reader is referred to Reference 8. Apart from these synthesis methods, various processing methods for discovering new bulk metallic glass compositions have also been developed in recent years. The high-temperature centrifugation method,[54,55] for example, can in multicomponent alloys physically isolate deep eutectic compositions, which have a high potential for good glass-forming ability.

17.2 Microstructure of Metallic Glasses

It has been shown that different processing techniques generate different atomic structure and free volume in metallic glasses, and that these differences are very sensitive to the cooling rates with which they are

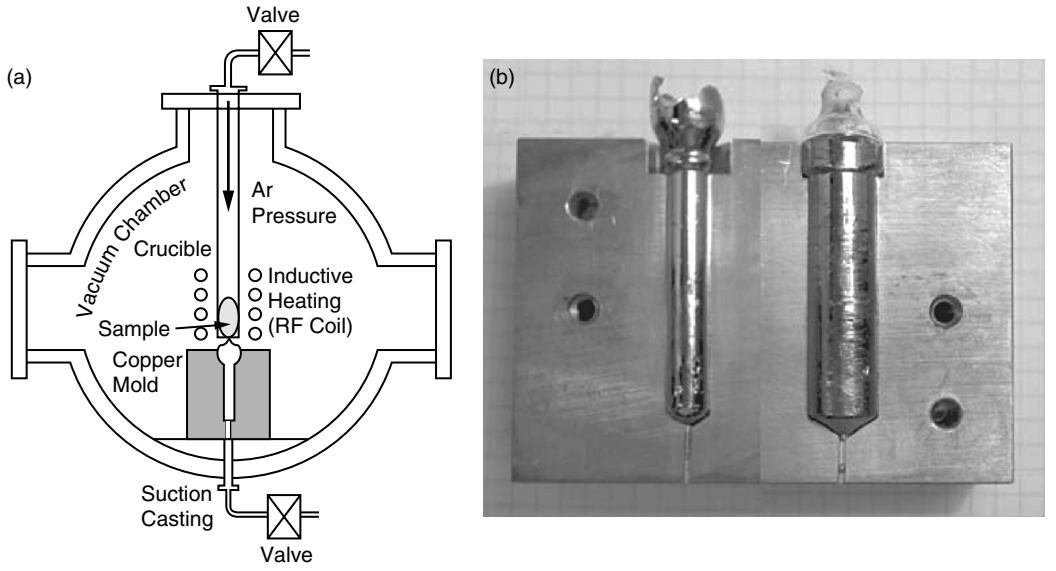

FIGURE 17.5 (a) Schematic drawing of a casting box, in which the samples are inductively heated and cast by either suction or pressure injection; (b) close-up photograph of a copper mold with cast Zr-based bulk metallic glass samples of diameters 5 and 10 mm.

produced. This in turn can have a drastic effect on mechanical and other physical properties: Mg-based bulk glasses, for example, are brittle if cast into larger samples, but bend in a ductile manner if produced at higher cooling rates.[56] To highlight this strong relationship between microstructure, processing, and properties we present some experimental methods for determining the microstructure of metallic glasses, point out the most relevant atomic models, and classify bulk metallic glasses according to their atomic structure.

17.2.1 Atomic Models for Metallic Glasses

17.2.1.1 Experimental Methods

Rapidly solidified amorphous alloys, as opposed to crystalline equilibrium alloys, are in a metastable state of nonperiodic atomic arrangement. This gives rise to typical diffuse rings in two-dimensional diffraction patterns, as shown in Figure 17.6a, or broad humps in a powder diffraction pattern (Figure 17.6b). In high-resolution transmission electron microscopy (HR-TEM) such metallic glasses show an irregular contrast resulting from the lack of any long-range periodicity in their atomic structure (Figure 17.6c). Metallic glasses show, however, some atomic short-range order on a length scale that is similar to the constituent atoms. The methods generally used to accurately detect such atomic short-range order are synchrotron radiation or neutron diffraction experiments.[57]

Using these techniques, the radial distribution function (RDF), describing the probability of interatomic distances, can be derived. Here the scattering vector **Q** arising from the x-ray diffraction of the amorphous solid is described by

$$Q = |\mathbf{Q}| = \frac{4\pi}{\lambda} \sin\theta, \tag{17.4}$$

where θ is the diffraction angle and λ is the x-ray wavelength. The atom–atom interference function, $S(Q)$, is derived from the total scattering intensity after subtraction of inelastic x-ray (Compton scattering) and

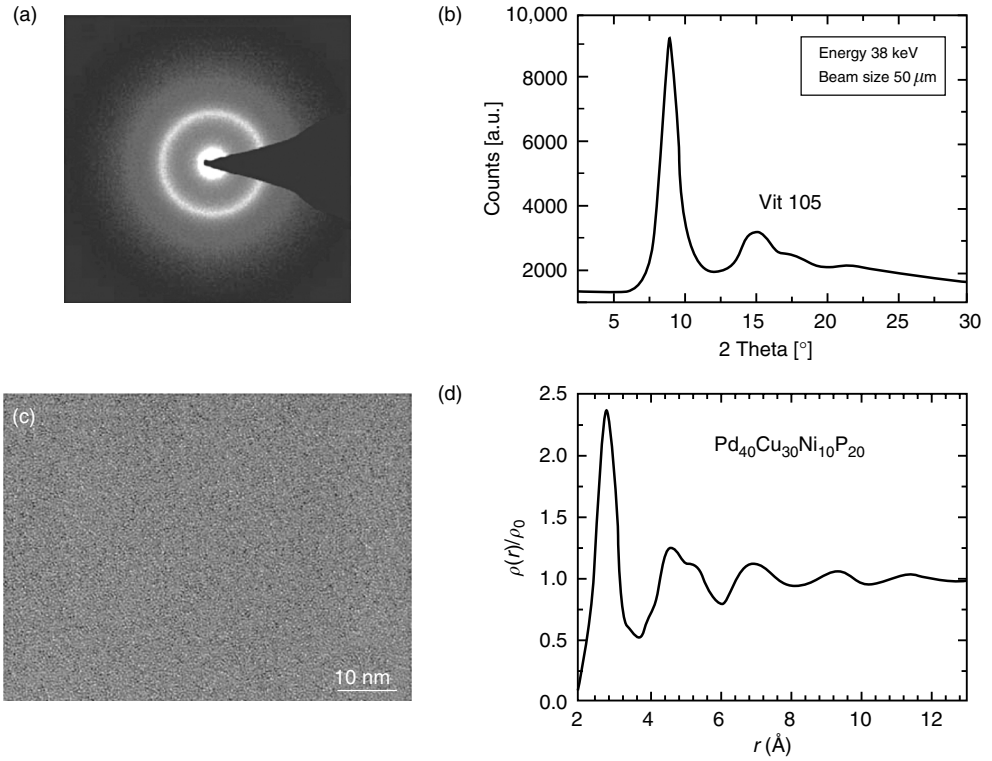

FIGURE 17.6 (a) Selected-area electron diffraction pattern of $Zr_{52.5}Ti_5Cu_{17.9}Ni_{14.6}Al_{10}$ (Vit105); (b) transmission synchrotron x-ray diffraction pattern of Vit105; (c) high-resolution transmission electron microscopy image of La–Cu–Al-based metallic glass; (d) normalized pair distribution function of amorphous $Pd_{40}Cu_{30}Ni_{10}P_{20}$. (17.6d from Yavari, A.R. et al., *Acta Mater.* 53, 1611, 2005. With permission.)

multiple scattering intensities,[58] that is

$$S(Q) = \frac{I(Q)}{\langle f(Q)\rangle^2} + 1 - \frac{\langle f(Q)^2\rangle}{\langle f(Q)\rangle^2}, \tag{17.5}$$

where $I(Q)$ is the normalized elastic scattering intensity after corrections for polarization and absorption, $f(Q)$ is the atomic scattering factor and $\langle \ldots \rangle$ refers to the composition average.[57] After normalizing $S(Q)$ to unity for large **Q** vectors, the atomic pair distribution function (PDF), $\rho(r)$, is obtained by Fourier transformation of $S(Q)$,

$$\rho\,(r) = \rho_0 + \frac{1}{2\pi^2 r}\int_{Q_{min}}^{Q_{max}} Q\,[S(Q) - 1]\sin(Qr)dQ, \tag{17.6}$$

where ρ_0 is the average atomic number density, $4\pi r^2\rho(r)$ is the RDF,[58–60] and the area under the first peak in the RDF provides the nearest-neighbor coordination number (see Figure 17.6d).[57] More recently, anomalous x-ray scattering techniques (measurement of the electron–photon resonance at the absorption edge), HR-TEM and TEM convergent-beam or nano-beam diffraction experiments have also been successfully applied to tackle the atomic structure of bulk metallic glasses experimentally.[10,61,62] Based on these and earlier results on the amorphous structure of solids and liquids, theoretical models were derived to assess the topology of the atomic structure.

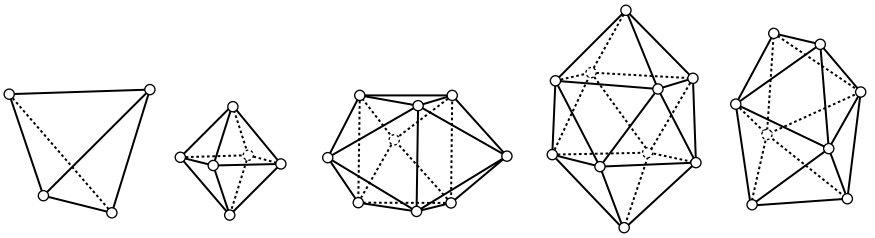

FIGURE 17.7 Bernal's "canonical holes," representing the different polyhedral void structures. These are tetrahedron, octahedron, trigonal prism, Archimedian anti-prism, and tetragonal dodecahedron (from left to right). (After Bernal, in Cahn, R.W. [Chap. 28], in *Physical metallurgy*, Cahn, R.W. and Haasen, P. (Eds.), Elsevier Science, New York, 1983, p. 1779. With permission.)

17.2.1.2 Theoretical Models

Due to the long-range order in crystalline solids all atoms form part of a unit cell, the latter being the smallest volume of atoms that can be translated along a lattice vector in the crystal without causing any overlap. Glasses, in contrast, can only be described in a statistical manner because of their lack of long-range order, and the RDF or PDF reflects the likelihood of finding the center of an atom in a distance r from a central atom. Therefore, models and simulations where the structure is precisely known and from which simulated PDFs may be derived and compared to experimental results are essential for an understanding of the structure of glassy solids and liquids.

Hard sphere models applied to crystalline solids have shown the closest packing orders for fcc and hexagonal closed-packed (hcp) structures, where in a 3-D space each sphere is coordinated by its 12 nearest neighbors, yielding a packing efficiency of 0.74. The void structure between the spheres forms tetrahedrons or octahedrons. In glassy materials, however, atoms are *randomly closed packed*. Bernal's[63–65] empirical model, the *dense random packing hard sphere* (DRP-HS) model, based on the structure of hard steel balls filling an irregular surface, yielded a packing efficiency much reduced compared to hcp and fcc structures of 0.60 to 0.63. The average likelihood of atomic positions resulted in a nearest-neighbor coordination number of 14.25 atoms and separated voids of different polyhedral shapes, whose vertices are defined by the (atomic) sphere centers, as shown in Figure 17.7. Polyhedral coordinated atomic clusters defined by Bernal's so-called "canonical holes" and the nearest-neighbor atoms can also be imagined.[66,67]

Regardless of the fairly good match of the PDF derived from the DRP-HS model with that of experimentally measured PDFs (e.g., on amorphous $Fe_{40}Ni_{40}P_{14}B_6$[68]), the DRP-HS model yields an unrealistically low density. This led to a modification of the DRP-HS model, which was consequently replaced by a *soft sphere model* increasing the packing efficiency to 0.69 to 0.70, in closer agreement with density measurements of amorphous metals and the observed PDFs.[69,70]

Despite this agreement with the experimental results for metallic glasses, the deficiency of these purely geometrical DRP models in being unable to cope with smaller metalloid atoms (whose presence generally improves glass-forming ability) and any variation in chemistry led to the so-called *local cluster models* (see, e.g., Reference 71). These models are particularly important for bulk metallic glasses, as they take into account the large variety of atomic species of different atomic diameter needed to frustrate crystallization. Following the proposal of Polk,[72] where small atoms such as those coming from metalloids (MO) fill the larger Bernal holes without distorting the DRP skeleton (formed by the larger transition metal [TM] atoms), Gaskell[70] showed that this was only possible if the smaller MO atoms had a diameter ≤ 0.48 that of the larger TM atoms. Such a structure is only possible for atoms like carbon and boron, but not for phosphorous or silicon. Gaskell therefore proposed a model where atoms are oriented in prisms analogous to the smallest stable crystalline phase.[70] Metallic glasses consisting of TM and MO atoms were thus suggested as forming clusters of cupped trigonal prisms among MO, which are loosely interconnected and possess orientations strongly dependent on the TM–MO attraction and their size. Today Gaskell's *network model*[70] is still applied to TM–MO glassy metals (see also next section) and has been proven to reflect satisfactorily the experimentally deduced PDFs for various bulk metallic glass systems.[73,74]

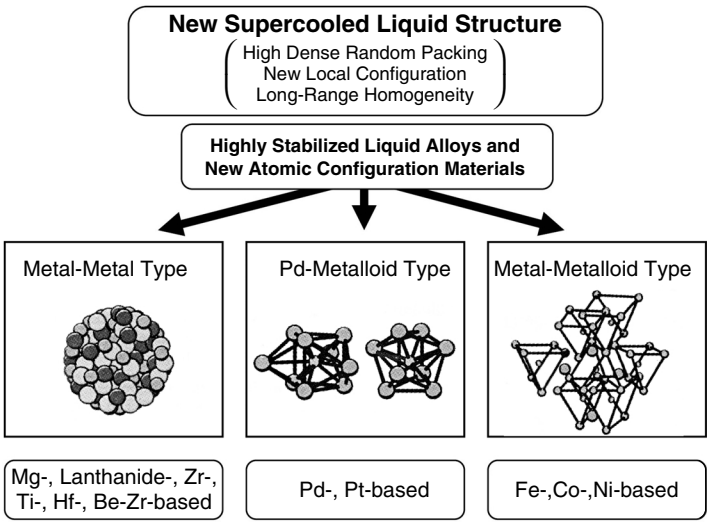

FIGURE 17.8 Classification of bulk metallic glasses according to their difference in local topological order. (From Inoue, A. and Takeuchi, A., *Mater. Trans. JIM* 43, 1892, 2002. With permission.)

17.2.2 Modern Classification

The findings concerning the atomic structure of amorphous alloys helped researchers to elaborate several rules with the goal of improving glass-forming ability,[9,11,75–78] leading to a decrease in the critical cooling rate and consequently to the generation of new bulk metallic glasses. The most-cited rules aiming to suppress crystallization are given in Reference 76, and can be summarized as follows: (1) the alloys must be composed of at least three elements; (2) the atomic size ratio of the constituent elements must be above 12%; and (3) a negative mixing enthalpy between the different elements must be present.

In an attempt to classify the wide range of recently-developed bulk metallic glasses, Inoue distinguished between three main groups. These are separated according to their chemical compositions and different atomic configurations into metal–metal-type alloys, metal–metalloid-type alloys (e.g., Fe–B or Ni–P), and Pd–metalloid-type alloys (see Figure 17.8).[79,80]

Experimental studies on the atomic structure of *metal–metal-type bulk metallic glasses* such as Zr–Al–Ni–Cu, Hf–Al–Ni–Cu and Zr–Ti–Cu–Ni–Be systems by means of HR-TEM, XRD, and neutron diffraction revealed an atomic structure consisting of icosahedral clusters,[61,62,81–85] as already suggested much earlier for liquids.[86] It was shown that an icosahedron is more stable than an fcc structure, because for a cluster of 13 atoms an icosahedron is connected through tetrahedrons making up 42 bonds, while an fcc structure is built by an octahedron and tetrahedron resulting in only 36 bonds.[81] On a local level where the nearest-neighbor atoms are bonded the stability is a function of the number of bonds, which can be increased by forming triangles in two dimensions and tetrahedrons in three dimensions. This leads to a geometric incompatibility in metallic glasses, because on a macroscopic level a 3-D structure consisting solely of tetrahedrons is, due to the strong mismatch and distortion energy required, less favorable than a mixture between tetrahedrons and octahedrons (i.e., closed-packed structure). This contributes to the stability of the glassy structure, as atoms do not know which configuration they should take.[87] Icosahedral structures have also been found in the supercooled liquid region of bulk metallic glass alloys prior to crystallization,[61,82,83,88,89] which may be explained by the lower activation energy needed for the nucleation of an icosahedral phase than for a closed-packed one.[90]

As mentioned earlier, *metal–metalloid-type systems* such as Fe–Lanthanide–B and Fe–M–B (M = Zr, Hf, Nb, Ta) consist of trigonal prisms where the smaller metalloids are located inside a skeleton made up by the TM atoms.[70] More recent studies on bulk metallic glasses consisting of TM–MO have (as for conventional TM–MO glasses) shown that the structure can be satisfactorily described by a variation of

the DRP model. Consequently, such structures exhibit higher densities than metal–metal-type metallic glasses.[73,74]

Pd–metalloid-type bulk metallic glasses, among which the Pd–Cu–Ni–P system shows the highest glass-forming ability of all bulk metallic glasses, are composed mainly of two large structures: transformed tetragonal dodecahedrons, which comprise Pd, Cu, and P, and trigonal prisms capped with three half-octahedral polyhedrons occupied by Pd, Ni, and P.[10] The significantly greater stability of the supercooled liquid and therefore the improved glass-forming ability of the Pd–Cu–Ni–P system compared to that of Pd–Ni–P, the latter built by trigonal prism clusters only, has been associated with the difficulty of rearranging the two clusters in a crystallographically ordered structure, their stable coexistence, and the high bonding strength of metal–metalloid atomic pairs in the cluster units.[10]

17.3 Thermophysical Properties of Metallic Glasses

As mentioned above, metallic glasses are amorphous metals quenched from the liquid state at a rate high enough to suppress crystal nucleation and growth. In this section, the rate of nucleation and growth will be derived as a function of undercooling. It will become evident why the reduced glass transition temperature T_{rg} (see Figure 17.2) and other parameters such as viscosity and fragility are important in describing glass-forming ability. In the context of homogenous nucleation and growth, a time–temperature–transformation (TTT) diagram for undercooled liquids is described theoretically and then compared to experimental data. The TTT diagram provides the basis for understanding how metallic liquids need to be processed to form bulk metallic glass parts.

17.3.1 Nucleation Rate and the Ability to Form a Glass

The ability to form a glass by cooling from an equilibrium liquid is equivalent to suppressing crystallization within the undercooled liquid. If a liquid is cooled below the melting point, the free energy difference between liquid and crystal will provide a driving force for crystal nucleation, while the creation of the liquid–crystal interface will create a positive interfacial energy that disfavors nucleation. This results in an energy barrier that a local composition fluctuation must overcome to form a nucleus. Easily derived, for a spherical nucleus this energy barrier is

$$\Delta G^* = \left(\frac{16\,\pi\,\gamma^3}{3\,(\Delta G_v)^2} \right), \tag{17.7}$$

where ΔG_v is the difference in Gibbs free energy (per unit volume) between liquid and crystal, and γ is the interfacial energy (per unit area).[25]

ΔG_v can be calculated from the difference in molar heat capacity at constant pressure between liquid and solid, Δc_p^{l-x}, the molar enthalpy of fusion (at the melting temperature), ΔH_m^f, the molar entropy of fusion, $\Delta S_m^f (= \Delta H_m^f / T_{liq})$ and the liquidus temperature, T_{liq}, by (e.g., Reference 91)

$$\Delta G_v(T) = \frac{1}{V_m} \left\{ \left(\Delta H_m^f - \int_T^{T_{liq}} \Delta c_p^{l-x}\left(T'\right) \mathrm{d}T' \right) - T \left(\Delta S_m^f - \int_T^{T_{liq}} \frac{\Delta c_p^{l-x}\left(T'\right)}{T'} \mathrm{d}T' \right) \right\}. \tag{17.8}$$

All the variables in the formula can be derived from quantitative heat capacity measurements using differential scanning calorimetry.

Experimental data concerning the molar Gibbs free energy difference, $\Delta G^{l-x}(T) = V_m \Delta G_v(T)$, with V_m the molar volume, are given in Figure 17.9 for selected metallic glasses.[92] The various alloys show different increases in ΔG^{l-x}. The best glass-formers, $Pd_{43}Cu_{27}Ni_{10}P_{20}$ (R_c = 0.2 K/s; Reference 93) and $Zr_{41.2}Ti_{13.8}Cu_{12.5}Ni_{10}Be_{22.5}$ (1 K/s; Reference 94), clearly show a flatter increase in ΔG_v with relative

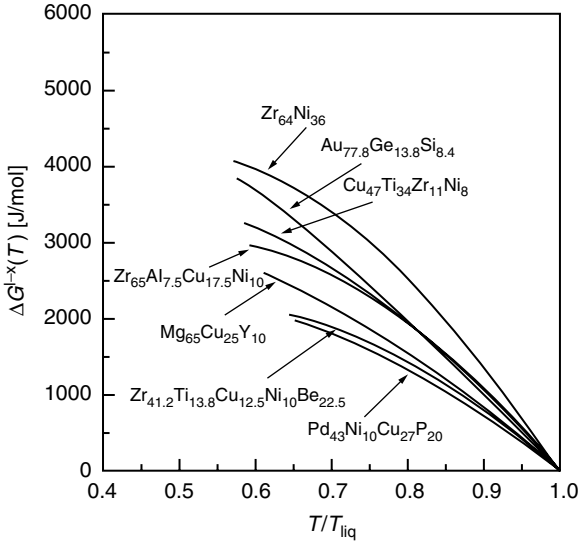

FIGURE 17.9 Molar Gibbs free energy differences between liquid and crystal $\Delta G^{l-x}(T) = V_m \Delta G_v(T)$ as a function of temperature for various metallic glass-forming melts. (From Fan, G.J., Löffler, J.F., Wunderlich, R.K., and Fecht, H.J., *Acta Mater.* 52, 667, 2004. With permission.)

undercooling, $\Delta T_r = 1 - (T/T_{liq}) = 1 - T_r$, than the marginal glass-former $Zr_{64}Ni_{36}$ ($R_c = 10^5$ K/s). The glass-formers $Mg_{65}Cu_{25}Y_{10}$, $Zr_{65}Al_{7.5}Cu_{17.5}Ni_{10}$, $Cu_{47}Ti_{34}Zr_{11}Ni_8$ and $Au_{77.8}Ge_{13.8}Si_{8.4}$ with critical cooling rates from 50 to 10^4 K/s lie in between.

In the following the temperature dependence of the Gibbs free energy difference is approximated as a function of undercooling, that is

$$\Delta G_v = \zeta(T) \frac{\Delta S_m^f}{V_m} (T_{liq} - T) = \zeta(T) \frac{\Delta H_m^f}{V_m} \Delta T_r, \tag{17.9}$$

where $\zeta(T)$ is a temperature-dependent correction factor that decreases slowly from 1 at T_{liq} to $\sim$0.7 at T_g.

The nucleus must form statistically by random atomic movement into a close-packed structure within the liquid. If the nucleus is smaller than the critical radius $r^* = 2\gamma/\Delta G_v$, the nucleus will dissolve. If, however, the nucleus is (in a few rare cases) larger than r^* the total free energy decreases with the size of the nucleus, and the latter is able to grow. The resulting crystal nucleation rate per unit volume, I_v, is thus the product of a thermodynamic term that depends on the probability of a fluctuation to overcome the nucleation barrier, and a kinetic term that depends on the atomic transport (described by the atomic diffusivity, D, or viscosity, η), that is,

$$I_v = \frac{A_v}{\eta(T)} \exp\left(-\frac{\Delta G^*}{k_B T}\right), \tag{17.10}$$

where A_v is a constant on the order of 10^{32} Pa s/(m^{3}s) and k_B is the Boltzmann constant.

Introducing the dimensionless parameters

$$\tilde{\alpha} \equiv \frac{(N_A V_m^2)^{1/3} \gamma}{\zeta(T) \Delta H_m^f} \quad \text{and} \quad \tilde{\beta} \equiv \frac{\zeta(T) \Delta S_m^f}{R}, \tag{17.11}$$

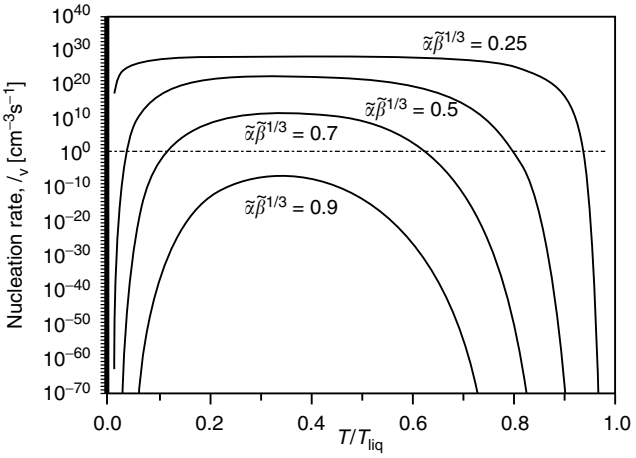

FIGURE 17.10 Homogeneous nucleation rate (Equation 17.14) as a function of reduced temperature with $\tilde{\alpha}\tilde{\beta}^{1/3}$ as parameter and $A_v/\eta = 10^{29}$ cm^{-3}s^{-1}. The dotted line indicates the range where one nucleus forms per second in a sample of volume $V = 1$ cm^3. This may be taken as the upper limit for obtaining a metallic glass by quenching.

where N_A is Avogadro's constant and R is the gas constant, the combination of Equation 17.7 and Equations 17.9–17.11 results in a nucleation rate of

$$I_v = \frac{A_v}{\eta} \exp\left(-\frac{16\pi}{3}\frac{\tilde{\alpha}^3\tilde{\beta}}{(\Delta T_r)^2 T_r}\right). \tag{17.12}$$

For metals, $\tilde{\alpha} \approx 0.4$–$0.5$, as $\gamma \approx 0.1$–0.5 J/m^2 and $\Delta H_m^f \approx 10$ kJ/mol (setting $\zeta(T) \approx 1$). Further, $\tilde{\beta} \approx 1$, as $\Delta S_m^f \approx R$. For nonmetals, $\tilde{\alpha} \approx 1/3$ and $\tilde{\beta}$ typically varies from 4 to 10.[95]

To obtain an upper bound for the nucleation rate, we first assume a constant viscosity of 10^{-3} Pa s, which is a typical value for the equilibrium melt viscosity of a metal, and plot the nucleation rate as a function of the reduced temperature $T_r = T/T_{liq}$ with $\tilde{\alpha}\tilde{\beta}^{1/3}$ as a parameter (Figure 17.10). For metals, $\tilde{\alpha}\tilde{\beta}^{1/3} \approx 0.4$ to 0.5; for nonmetals, $\tilde{\alpha}\tilde{\beta}^{1/3} \approx 0.5$ to 0.7. Apparently, the nucleation rate rises steeply with increasing undercooling, but nucleation is often negligible down to $\Delta T_r \approx 0.2$.

A more realistic approach is to assume that the viscosity follows a Vogel–Fulcher-type temperature dependence, $\eta(T) = \eta_0 \exp[B/(T - T_0)]$. According to Angell's fragility concept,[96,97] the viscosity of liquids is commonly described by a modification of the Vogel–Fulcher–Tammann (VFT) relation,

$$\eta(T) = \tilde{\eta} \exp\left(\frac{D^* T_0}{T - T_0}\right), \tag{17.13}$$

where D^* is the fragility parameter ($1 \leq D^* \leq 100$), T_0 the VFT temperature, and $\tilde{\eta}$ a constant inversely proportional to the molar volume of the liquid. Physically, T_0 is the temperature where the barrier would become infinite with respect to flow. The fragility describes the degree to which the viscosity of a supercooled liquid deviates from an Arrhenius behavior. Liquids are commonly referred to as "fragile" when $D^* < 10$ and "strong" when $D^* > 20$. Strong liquids have a high equilibrium melt viscosity and show a more Arrhenius-like temperature dependence in the viscosity than fragile liquids. For pure metals, D^* is close to unity, while for the network glass SiO_2, the classical example of a "strong" glass former, $D^* = 100$. The viscosity of SiO_2 shows an Arrhenius-like temperature dependence.

According to this concept, Equation 17.12 takes, in dimensionless parameters, the form

$$I_v = \frac{A_v}{\tilde{\eta}} \exp\left(-\frac{D^* T_{r0}}{T_r - T_{r0}}\right) \exp\left(-\frac{16\pi}{3} \frac{\tilde{\alpha}^3 \tilde{\beta}}{(\Delta T_r)^2 T_r}\right), \tag{17.14}$$

where $T_{r0} = T_0/T_{liq}$ is the reduced VFT temperature. As has recently been shown, the VFT temperature T_0 is significantly lower than the glass transition temperature T_g, and can be as low as 0.6 T_g.[98] Nevertheless, we assume in the following that $T_{r0} \approx T_{rg}$ (with T_{rg} the reduced glass transition temperature) to obtain an upper bound for the nucleation rate.

Apparently there are two important parameters that determine the nucleation rate: the reduced VFT temperature T_{r0} (or reduced glass transition temperature T_{rg}), and the fragility parameter D^*. While there are many experiments that determine the fragility parameter in metallic glasses,[98] its influence on the nucleation rate has not so far been parameterized. We therefore take into consideration the reduced glass transition temperature T_{rg}, as did Turnbull[25] (see Figure 17.11a), and the fragility parameter D^* (see Figure 17.11b). To visualize the influence of T_{rg} on the nucleation rate, Figure 17.11a

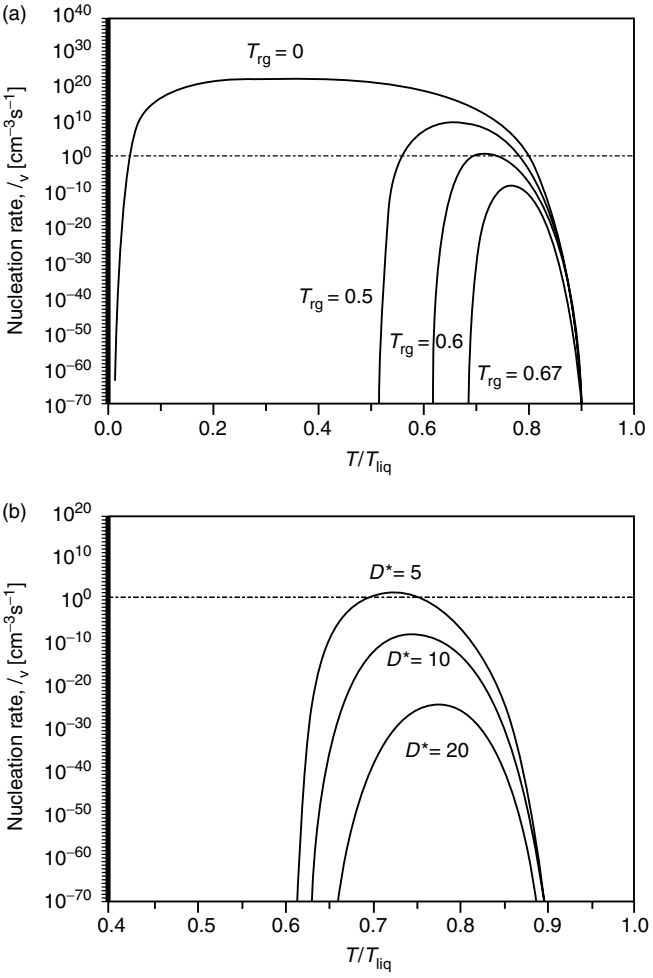

FIGURE 17.11 Homogeneous nucleation rate (Equation 17.14) as a function of the reduced temperature, with $\tilde{\alpha}\tilde{\beta}^{1/3} = 0.5$ and $A_v/\tilde{\eta} = 10^{-29}$ cm^{-3}s^{-1}. (a) $D^* = 5$ and T_{rg} ($\approx T_{r0}$) as parameter; (b) T_{rg} ($\approx T_{r0}$) = 0.6 and D^* as parameter.

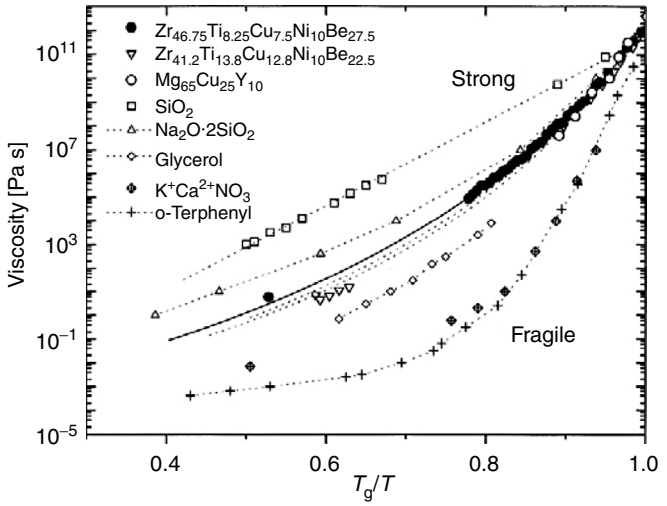

FIGURE 17.12 Fragility plot for various oxide glass-formers, organic glass-formers, and three metallic glass-formers. (Reproduced from Busch, R., Bakke, E., and Johnson, W.L., *Acta Mater.* 46, 4725, 1998. With permission.)

TABLE 17.1 Fragility Parameter, D^*, Critical Cooling Rate, R_c, and Reduced Glass Transition Temperature, T_{rg}, for Selected Metallic Glasses

Alloy	D^*	R_c [K s^{-1}]	T_{rg}	Additional Ref.
SiO_2	100	<0.1	0.67	
$Mg_{65}Cu_{25}Y_{10}$	23	20	0.68	103
$Zr_{41.2}Ti_{13.8}Cu_{12.5}Ni_{10}Be_{22.5}$ (Vit 1)	22.7	1	0.66	104
$Zr_{46.75}Ti_{8.25}Cu_{7.5}Ni_{10}Be_{27.5}$ (Vit 4)	20.4	18	0.62	98
$Pd_{48}Ni_{32}P_{20}$	15.1	10 (if fluxed)	0.66	105
$Zr_{65}Al_{7.5}Cu_{17.5}Ni_{10}$	13.8	50	0.60	
$Zr_{60}Ni_{25}Al_{15}$	11.6	10^2	0.60	32
$Pd_{77.5}Cu_6Si_{16.5}$	6.3	10^3	0.58	105
$Au_{77.8}Ge_{13.8}Si_{8.4}$	8.4	10^5	0.55	106
$Zr_{64}Ni_{36}$	7.9	10^6	0.50	

Source: Modified after Johnson, W.L., in *Science of Alloys for the 21st Century: A Hume-Rothery Symposium Celebration*, P.E.A. Turchi, R.D. Shull and A. Gonis (Eds.), The Minerals, Metals & Materials Society, 2000. With permission.

shows the nucleation rate as a function of the reduced temperature $T_r = T/T_{liq}$ with $\tilde{\alpha}\tilde{\beta}^{1/3} = 0.5$, $A_v/\tilde{\eta} = 10^{-29}$ $cm^{-3}s^{-1}$, and $D^* = 5$. To visualize the influence of D^*, Figure 17.11b shows the nucleation rate as a function of the reduced temperature T_r with $\tilde{\alpha}\tilde{\beta}^{1/3} = 0.5$, $A_v/\tilde{\eta} = 10^{-29}$ $cm^{-3}s^{-1}$, and $T_{rg} = 0.6$. Apparently, while fragile liquids with $D^* \leq 5$ crystallize when $T_{rg} = 0.6$, stronger liquids with $T_{rg} = 0.6$ can be quenched into a glass.

By fitting the VFT relation (Equation 17.13) to experimental data, values of $D^* = 22.7$ and $T_0 = 372$ K were obtained for the alloy $Zr_{46.75}Ti_{8.25}Cu_{7.5}Ni_{10}Be_{27.5}$.[98] The viscosity data as a function of T_g/T is visualized in the fragility plot[97] in Figure 17.12. The viscosity data were derived from beam-bending experiments up to a temperature of 100 K above T_g[99] and from additional melt viscosity data.[100] As the timescales for the experiments at temperatures between T_g and T_{liq} are very short, noncontact measurement techniques have also recently been used to study the viscosity of undercooled liquids.[101]

Table 17.1 shows experimental data for D^* and the critical cooling rate of several metallic glass-forming alloys. The data show that good glass-formers indeed have a high fragility index of $D^* > 20$.

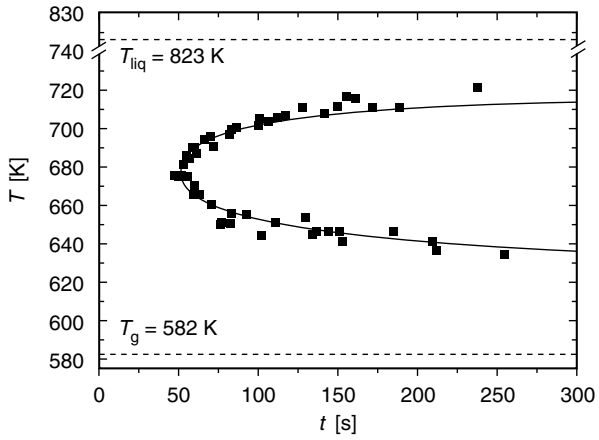

FIGURE 17.13 Time–temperature–transformation (TTT) diagram of the bulk metallic glass-former $Pd_{40}Cu_{30}Ni_{10}P_{20}$. (Reproduced from Löffler, J.F., Schroers, J., and Johnson, W.L., *Appl. Phys. Lett.* 77, 681, 2000. With permission.)

17.3.2 Time–Temperature–Transformation Diagrams

Crystallization in the undercooled melt preferably sets in if the temperature is low enough to result in sufficient undercooling (resulting in an increasing thermodynamic driving force for nucleation) and if it is high enough to allow sufficient atomic mobility. The onset times plotted for different temperatures form a typical nose-type curve with the so-called "nose temperature" at the shortest crystallization time, a lower branch representing decreasing kinetics, and a higher branch representing decreasing undercooling or decreasing driving force for nucleation when moving away from the nose temperature (see Figure 17.13). Stable metallic glasses, such as Vit 1 ($Zr_{41.2}Ti_{13.8}Cu_{12.5}Ni_{10.0}Be_{22.5}$) or $Pd_{40}Cu_{30}Ni_{10}P_{20}$, reach incubation times at the nose temperature of ~50 s.[94,107] The experiments are usually performed using containerless levitation techniques, for example, electrostatic levitation,[108] or in graphite crucibles using B_2O_3 flux.

The crystallization times can be fitted using the Johnson–Mehl–Avrami model.[109,110] For low values of crystallized volume fraction, f, the crystallization time, t, is

$$t = \left(\frac{3f}{\pi \; I_v v^3} \right)^{1/4}, \tag{17.15}$$

with the nucleation rate, I_v, given by Equation 17.12 and the growth velocity, v, given by

$$v = \frac{D}{l} \left\{ 1 - \exp\left(- \frac{(V_m/N_A)\, \Delta G_v(T)}{k_B T} \right) \right\}. \tag{17.16}$$

Here the diffusivity, D, may be related to the viscosity via the Stokes–Einstein relation $D = k_B T/(3\pi\eta(T)l)$, with l the (average) atomic diameter. Using measured values for the temperature dependence of the viscosity, $\tilde{\eta} = 9.34 \times 10^{-3}$ Pa s, $D^* = 9.25$ and $T_0 = 447$ K,[111] using the approximation $V_m \Delta G_v \approx \Delta S_m^f (T_{liq} - T)$ with $\Delta S_m^f = 8.55$ J/(mol K) and $T_{liq} = 823$ K, estimating the detectable volume fraction of crystals, f, to be ~0.5%, and using $l \approx 3.1$ Å, the curve in Figure 17.13 can be fitted to the data using A_v and γ as fitting parameters. The fit shown in Figure 17.13 gives $A_v = 4.4 \times 10^{31}$ Pa s/(m^3 s) and $\gamma = 0.067$ J/m^2. The latter is comparable to values for monatomic liquids with low melting temperature (e.g., $\gamma = 0.058$ J/m^2 for Cd and 0.108 J/m^2 for Al).

Quenching of a melt into a metallic glass can be seen as cooling it fast enough to pass from T_{liq} to T_g without crossing the nose-shaped crystallization curve. In this respect continuous–cooling–transformation diagrams (CCT) would be more suitable, but no experimental CCT diagrams have so

far been reported. Note that for different primary crystallizing phases, different crystallization curves need to be drawn into the TTT diagram. This (together with a possibility of phase separation in the deeply undercooled liquid region[112–114]) is one of the reasons why the TTT diagram of Vit1 could not be successfully fitted with the procedure described above over the entire temperature range.[94]

17.3.3 Processing Possibilities

As outlined in Section 17.3.2, a metallic glass can be produced if the liquid is cooled quickly enough to bypass the nose of the TTT diagram. In principle there are two processing methods, as shown schematically in Figure 17.14.

In the "injection casting" procedure, the glass-forming melt is processed directly from the melt into its final shape, as shown in Figure 17.14a. The melt is first undercooled to a temperature below the nose at a cooling rate high enough to bypass the nose of the TTT diagram. Then, at the temperature below the nose (but above the glass transition temperature T_g), the material can be injected in a way similar to polymer melts, as the viscosity is higher than in conventional melts but still low enough ($<10^8$ Pa s) to allow for injection molding. It is interesting to note that with suitable processing equipment and process control, the injection casting method can deliver glassy parts with larger dimensions than the critical casting thickness, d_c, of their constituent material: for example, the glass-forming liquid can be cooled quickly to a temperature below the nose (e.g., by flowing through various thin, water-cooled channels with $d < d_c$) and then injection-cast into a part with $d > d_c$ at a temperature above T_g.

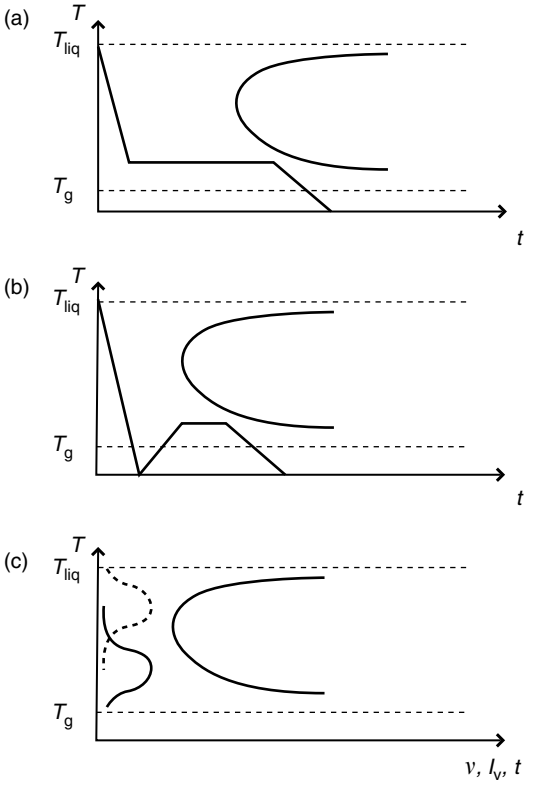

FIGURE 17.14 Schematic TTT diagrams and processing possibilities for metallic glasses in the undercooled liquid regime: (a) upon cooling from the melt ("injection casting") and (b) upon heating of a glass ("superplastic forming"). (c) Different temperatures for maxima of growth rate, v, (dashed) and nucleation rate, I_v, (solid line), explaining that the processing times in "injection casting" (a) are generally higher than in "superplastic forming" (b).

The "superplastic forming" process is shown schematically in Figure 17.14b. Here the glass-forming melt is quenched into a glass (i.e., to a temperature below T_g) at a cooling rate high enough to suppress crystallization. The glassy material can then be stored as feedstock material (in the form of small spheres, for example) at room temperature for extended periods of time without any effect on the microstructure. For processing in the supercooled liquid, the material is then heated to a temperature above T_g (but below the nose temperature) and formed.

As shown in Figure 17.14, the TTT diagrams differ for the processes of injection molding and superplastic forming, respectively. This is because crystallization in undercooled liquids is history-dependent, that is, different crystallization times exist at one temperature T depending on whether the temperature is reached by heating of the glass or undercooling of the melt.[115] This asymmetry results from the fact that the thermodynamic driving force for nucleation increases with increasing undercooling, while the kinetics simultaneously decreases. Consequently, there exist different temperatures for the maxima for growth rate and nucleation rate, as shown schematically in Figure 17.14c. As nucleation is the rate-dominating step for crystallization, the TTT diagram of "injection casting" (Figure 17.14a) generally shows longer crystallization times than that of "superplastic forming" (Figure 17.14b).

17.4 Processing in the Undercooled Liquid Region

17.4.1 Thermal Stability and Formability

For processing metallic glasses in the undercooled liquid, the onset of crystallization is the limiting factor. A measure for the stability of the undercooled liquid upon heating is the extension of the undercooled liquid regime, $\Delta T = T_x - T_g$, usually measured in differential scanning calorimetry (DSC) experiments performed at a certain heating rate, with T_x the first crystallization temperature (Figure 17.15). Despite the fact that thermal stability and glass-forming ability are not necessarily correlated,[116,117] conventional metallic glasses usually show only a small undercooled liquid region of $\Delta T \lesssim 20$ K (or show no glass transition at all), while the more recently developed bulk metallic glasses generally exhibit a large undercooled liquid regime of 50 K $< \Delta T <$ 150 K. It is this extension of the undercooled liquid range that enables bulk metallic glasses to be superplastically formed (from a feedstock material) in a way similar to polymers.

For current bulk metallic glasses, the processing temperature is, however, still a compromise between temperatures too high to suppress crystallization and too low to facilitate forming, as the viscosity increases

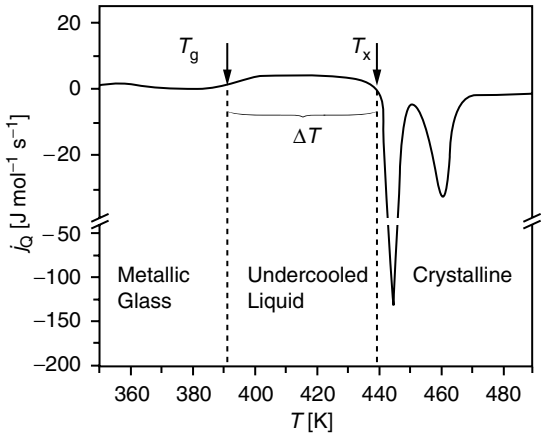

FIGURE 17.15 Differential scanning calorimetry scan of a metallic glass ($Au_{49}Ag_{5.5}Pd_{2.3}Cu_{26.9}Si_{16.3}$) with glass transition (T_g), crystallization temperature (T_x), and different regimes marked (positive j_Q values represent endothermic heat flow, measured at a heating rate of 10 K/min).

TABLE 17.2 Glass Transition Temperature, T_g, Thermal Stability, ΔT, Normalized Thermal Stability, ΔS, and Critical Casting Thickness, d_c, of Various Bulk Glass-Forming Alloys

Alloy	T_g(K)	ΔT(K)	ΔS	d_c(mm)	Ref.
$Ce_{68}Cu_{20}Al_{10}Nb_2$	341	81	0.26	8	119
$Au_{49}Ag_{5.5}Pd_{2.3}Cu_{26.9}Si_{16.3}$	401	58	0.24	5	120
$Mg_{58}Cu_{30.5}Y_{11.5}$	424	75	0.22	9	121
$La_{55}Ni_{20}Al_{25}$	472	73	0.16	3	122
$Pt_{57.5}Cu_{14.7}Ni_{5.3}P_{22.5}$	507	98	0.34	16	123
$Pd_{40}Cu_{30}Ni_{10}P_{20}$	577	95	0.37	72	124
$Zr_{44}Ti_{11}Cu_{10}Ni_{10}Be_{25}$	625	114	0.20	10	89
$Zr_{65}Cu_{15}Ni_{10}Al_{10}$	645	106	0.23	4	76

steeply with decreasing temperature and the maximum force to be applied during forming is often limited. This is particularly true for micro- and nanostructuring, where, for example, silicon molds with limited strength are used.

As the decrease in flow stress with temperature (above T_g) differs for the various alloys, it has been suggested that ΔT normalized to the temperature interval between T_g and the liquidus temperature T_{liq},

$$\Delta S = \frac{\Delta T}{T_{liq} - T_g}, \tag{17.17}$$

will estimate formability better than ΔT.[118] In Table 17.2 suitable alloys for superplastic forming representing different metallic systems are listed together with their values for T_g, ΔT, ΔS, and d_c.

The above-mentioned parameters for the stability of metallic glasses do not take into account the viscosity of the undercooled melt. It has indeed been shown that the viscosity at the crystallization temperature is lower for thermally less-stable glasses[125] (e.g., 10^5 Pa s for $Zr_{41.2}Ti_{13.8}Cu_{12.5}Ni_{10}Be_{22.5}$[3] and 7×10^5 Pa s for $Mg_{60}Cu_{30}Y_{10}$[126] with a lower ΔT of 55 and 60 K, respectively), but higher for thermally more stable glasses (e.g., 8×10^7 Pa s for $La_{55}Al_{25}Ni_{20}$[127] and 3×10^8 Pa s for $Zr_{65}Al_{10}Ni_{10}Cu_{15}$[128] with a larger ΔT of 70 and 105 K, respectively).

More exact forming properties that do take into account the various fragilities are obtained by measuring the flow stress of metallic glasses above the glass transition temperature. These measurements have been performed in detail on several alloys (see Section 17.5). The flow stress σ and the strain rate $\dot{\varepsilon}$ are related to the viscosity via

$$\eta = \frac{\sigma}{3\dot{\varepsilon}}. \tag{17.18}$$

The values described above for viscosity are good estimates of forming ability. For more detailed studies, however, dynamic measurements are required in which the viscosity is represented by a complex value,

$$\eta^* = \frac{G' + iG''}{\omega}, \tag{17.19}$$

where the real part of $\omega\eta^*$ is the storage modulus G', and the imaginary part of $\omega\eta^*$ is the loss modulus G''. Physically, G' represents the (time-independent) elastic contribution, while G'' represents the (time-dependent) viscous contribution for a given angular frequency, ω.

Figure 17.16a shows measurements of G' and G'' for the metallic glass $Ce_{68}Cu_{20}Al_{10}Nb_2$ as a function of temperature (measured at a heating rate of 10 K/min) using oscillating parallel plate geometry (not to be confused with earlier "parallel plate" indentation measurements).[129] Also shown is the modulus of the dynamic viscosity, $|\eta^*| = (1/\omega)\sqrt{(G')^2 + (G'')^2}$. Interestingly, the metallic glasses show a viscoelastic behavior in the superplastic regime with a dominant viscous component. Such dynamic viscosity measurements are particularly helpful for predicting the flow behavior in the forming of parts with complex

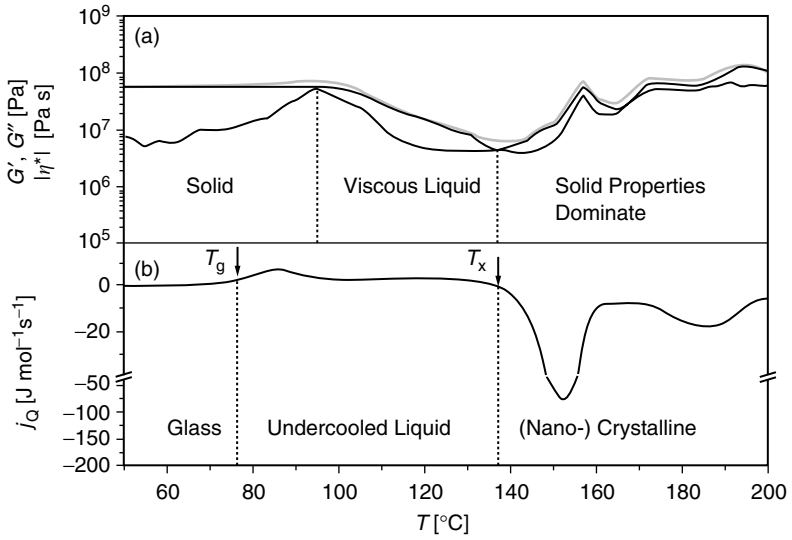

FIGURE 17.16 (a) Storage modulus (G'), loss modulus (G'') and absolute value of the dynamic viscosity ($|\eta^*|$) for the bulk metallic glass $Ce_{68}Cu_{20}Al_{10}Nb_2$; and (b) DSC trace for the same alloy, measured at a heating rate of 10 K/min.

geometries. To determine the structural changes during heating, a DSC curve has also been measured at the same heating rate as in the viscosity measurements, and is shown in Figure 17.16b.[129]

17.4.2 Injection Casting

Metallic glass-forming melts typically show a high melt viscosity and can be easily undercooled. Injection casting of such undercooled melt has several advantages: compared to crystalline alloys, the absence of crystallization shrinkage and of crystalline anisotropy in the final parts allows near-net-shape molding of parts with isotropic properties. In addition, the material exhibits homogenous properties on a length scale down to the nanometer range. As modern applications require parts in the micro- and nanometer range, the homogeneity of the material (e.g., the absence of grain boundaries) becomes crucial. Parts with micrometer-sized features or of complicated shape have been successfully prepared by injection casting of metallic glasses,[130] as shown in Figure 17.17. In addition, due to the available long processing times in the undercooled liquid regime, injection casting can deliver large parts in the range of several centimeters, as shown for example in Figure 17.18 (parts available commercially).

17.4.3 Superplastic Forming

The superplastic deformation behavior of metallic glasses above T_g is described by viscous flow (Newtonian or non-Newtonian; see Section 17.5.1) and should be distinguished from, for example, grain-boundary sliding or dynamic recrystallization in crystalline *superplastic* alloys.[131] More general details on superplasticity are given in Chapter 14.

One of the first successful superplastic forming experiments on metallic glasses was the extrusion of glassy $Zr_{65}Al_{10}Ni_{10}Cu_{15}$ metal powder at temperatures above T_g.[132] Here superplastic forming was possible because of the alloy's high thermal stability. This procedure generated the same mechanical properties as casting, which shows that superplastic forming in the undercooled liquid regime is possible without any degradation of the material's properties.

Superplastic forming of parts and surface structures in the micro- and nanometer range is also attracting great interest. Metallic glasses show good microformability, high strength, high elastic limit, and good corrosion properties combined with a homogeneity of the mechanical and chemical properties on the

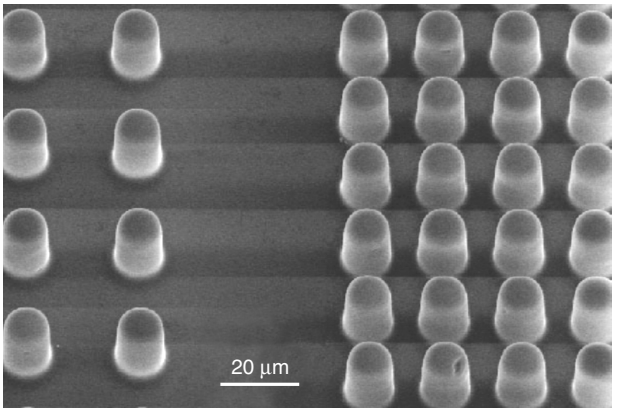

FIGURE 17.17 Pins of 20 μm in height and 8 μm in diameter of a bulk metallic glass, replicated from a surface-microstructured Si wafer by rapid cooling from the melt.

FIGURE 17.18 Photo of commercially available parts made of injection-molded metallic glass (SanDisk Cruzer® Titanium 512 MB USB memory stick and Liquidmetal® Technologies cell phone case).

micrometer and sub-micrometer scale due to the absence of grain boundaries.[133] The replication of surface topologies on the micrometer scale from, for example, silicon in metallic glasses by superplastic forming has been realized for $Zr_{46.8}Ti_{8.2}Cu_{7.5}Ni_{10}Be_{27.5}$ (Vit 4)[134] (see Figure 17.19), $Pt_{48.75}Pd_{9.75}Cu_{19.5}P_{22}$,[135] $La_{60}Al_{20}Ni_{10}Co_5Cu_5$[136] and $Pt_{57.5}Cu_{14.7}Ni_{5.3}P_{22.5}$.[118] With the Pt-based alloys, features in the range of 10 to 100 nm (with a low aspect ratio)[135] and a few micrometers (with a high aspect ratio)[118] were successfully replicated from silicon molds.

Superplastic forming can also be used to fabricate parts from metallic glass of a larger size than the critical cooling rate allows. If a feedstock material is first quenched in small droplets, these metallic glass billets can subsequently be forged into a large part. With the recent development of better glass-forming alloys, thermal stability has also increased, making superplastic forming of large parts similar to that of polymer materials feasible. Indeed, as can be seen in Figure 17.20, the forming of hand-size parts using pellets as feedstock material has already been realized with the alloy $Pt_{57.5}Cu_{14.7}Ni_{5.3}P_{22.5}$. Here the pellets were pressed into a cup for 100 s using a pressure of 20 MPa at a temperature of 260° C.[118]

17.4.4 Co-Extrusion with Polymers

With further development of metallic glasses and the resulting larger parameter ranges (wider range of T_g, higher thermal stability, lower critical cooling rates), additional processing methods will become available

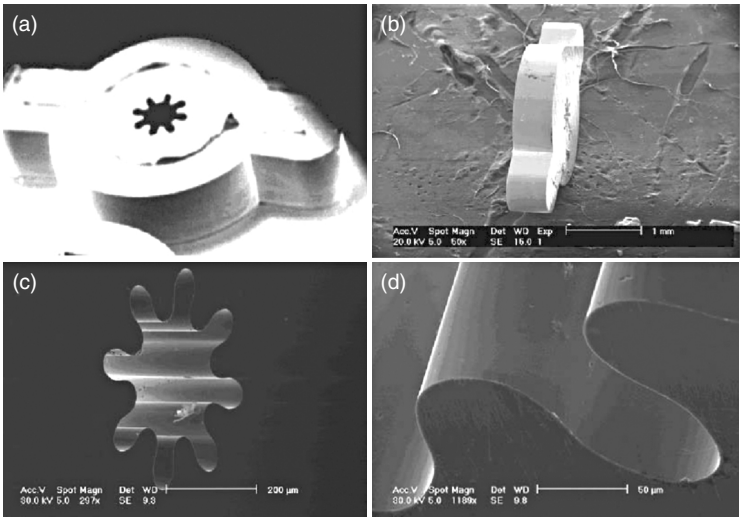

FIGURE 17.19 Microgears made of bulk metallic glass ($Zr_{46.8}Ti_{8.2}Cu_{7.5}Ni_{10}Be_{27.5}$, Vit 4) replicated from a $Ni_{85}Co_{15}$ mold by superplastic forging. (From Zumkley, T., Suzuki, S., Seidel, M., Mechler, S., and Macht, M.P., *Mater. Sci. Forum* 386–388, 541, 2002. With permission.)

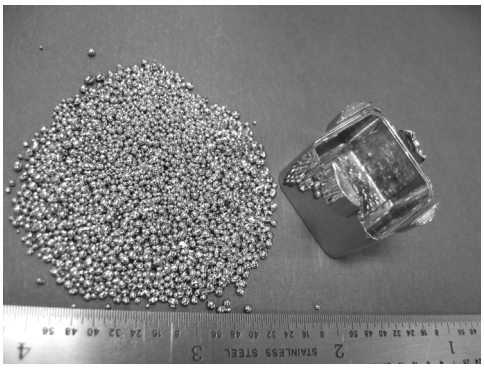

FIGURE 17.20 Feedstock material and superplastically formed part made of the metallic glass $Pt_{57.5}Cu_{14.7}Ni_{5.3}P_{22.5}$. (Reproduced from Schroers, J., *J. Mater. JOM* 57, 35, 2005. With permission.)

for metallic glasses. One of these could be the co-extrusion of metallic glasses and polymers to form composites. With the recent development of metallic glasses with a T_g in the range of that of polymers, the two can be processed at temperatures where they show the same viscosity. In Figure 17.21 the dynamic viscosities for various metallic glasses are shown upon continuous heating and compared with the zero viscosities (i.e., viscosities extrapolated to $\dot{\gamma} = 0$) of polymers, η_0.[129] The first drop in viscosity in the metallic glasses is the softening of the metallic glass above T_g. An additional drop is observed in the Mg and Ce alloys after the onset of crystallization. This may be due to a change in composition or density of the remaining amorphous phase after the onset of crystallization. As Figure 17.21 shows, the viscosities of polymers and metallic glasses match closely, allowing co-processing of the two with similar flow behavior. Thus, even with today's metallic glasses, polymer–metallic glass pairs with similar viscosities can be picked out and treated together (e.g., the Ce-based metallic glass $Ce_{68}Cu_{20}Al_{10}Nb_2$ and high-density polyethylene HDPE6021 at 120°C; or the Au-based metallic glass $Au_{49}Ag_{5.5}Pd_{2.3}Cu_{26.9}Si_{16.3}$ and polystyrene, PS, at 160°C). With the development of these new metallic glasses the production of metal/polymer composites via co-processing may become a simple method for interesting composite materials.

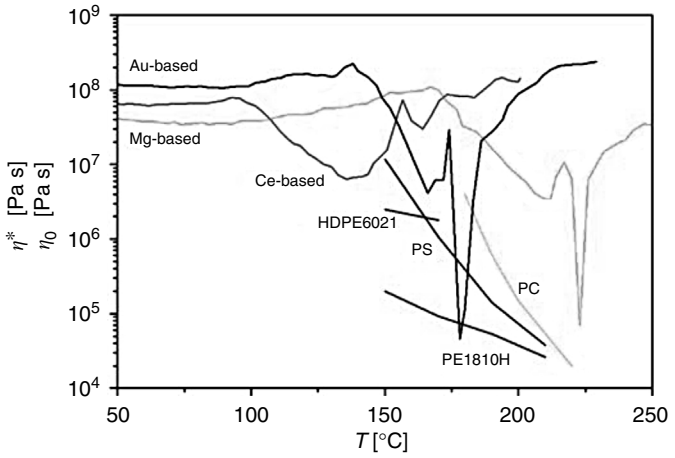

FIGURE 17.21 Dynamic viscosity data for three metallic glasses, Au-based ($Au_{49}Ag_{5.5}Pd_{2.3}Cu_{26.9}Si_{16.3}$), Ce-based ($Ce_{68}Cu_{20}Al_{10}Nb_2$) and Mg-based ($Mg_{58}Cu_{30.5}Y_{11.5}$) as a function of temperature (heating rate: 10 K/min). In addition, zero viscosities for four polymers are shown (HDPE6021: a high-density polyethylene; PE: low-density polyethylene; PS: polystyrene; PC: polycarbonate). Note that the zero viscosity for an amorphous material is slightly higher than the dynamic viscosity.

17.5 Mechanical Properties of Metallic Glasses

17.5.1 Introduction

In the earlier stages of research into metallic glasses, mechanical properties such as tensile strength, plastic deformation, fracture toughness and superplastic forming generated only minor interest due to the limited thickness of the glassy metal foils obtained.

Research into metallic glasses mostly concentrated on magnetic properties, due to their excellent soft-magnetic properties (explained by the so-called random-anisotropy model, e.g., References 137 and 138) and their potential commercial applications in transformer cores. However, with the advent of bulk metallic glasses in the 1990s, research into mechanical properties became increasingly important due to the potential of bulk metallic glasses as structural and functional materials. Here we describe the mechanical properties of bulk metallic glasses but exclude a description of their magnetic properties. (For overviews on the magnetism of metallic glasses we refer to References 26, 139, and 140. Some applications of magnetic glasses are, however, outlined in Section 17.7.1.)

The processing of metallic glass-forming liquids can strongly influence mechanical properties. It is thus important to understand the influence of deformation mode, temperature, and strain rate on the mechanical response of bulk metallic glasses. For instance, controlled processing can lead to a composite-type material, consisting of ductile dendritic crystals in a glassy matrix, which shows improved mechanical properties compared to the monolithic glass. Various production methods for bulk metallic glass composites are outlined in Section 17.6. In the current section, a general overview of the mechanical properties of bulk metallic glasses is presented, followed by a detailed discussion of their mechanical properties at ambient and elevated temperatures and a description of their inhomogeneous and homogeneous deformation behavior.

17.5.2 Temperature Dependence of Deformation in Metallic Glasses

At temperatures significantly lower than the glass transition temperature, T_g, plastic deformation is inhomogeneous and characterized by the propagation of a few highly localized shear bands. In contrast

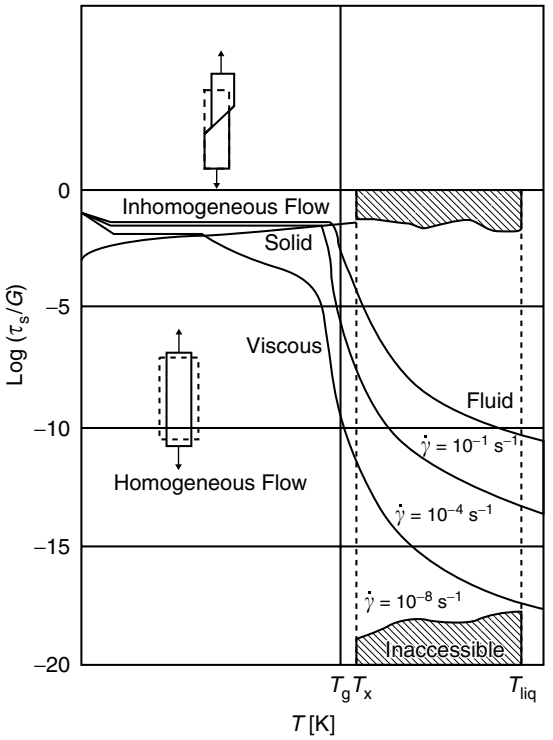

FIGURE 17.22 Deformation map (shear stress-temperature curve) for metallic glasses. Plotted is the normalized shear stress (shear stress divided by shear modulus) as a function of temperature, with the shear strain rate $\dot{\gamma}$ as parameter. (Reproduced from Spaepen, F., *Acta Metall.* 25, 407, 1977. With permission.)

to their crystalline counterparts, where resistance to plastic deformation is significantly lower due to the operation of 2-D lattice defects (dislocations), metallic glasses lack atomically even glide planes allowing for easy slip. Their disordered atomic arrangement represents a great obstacle to plastic deformation, such that slip is hindered unless very high stresses are applied which trigger the hopping of atoms and the diffusion of vacancy-like free volume, resulting in the formation of localized shear planes. In Spaepen's deformation map or stress-temperature diagram (Figure 17.22)[141] this deformation behavior generates a very low but negative slope, indicating that the shear or fracture stress decreases linearly with increasing temperature as the elastic modulus decreases.[142]

At temperatures close to T_g, plastic flow in metallic glasses becomes homogeneous and requires significantly lower stress than at lower temperatures. At low strain rates it is described by Newtonian viscous flow, where the viscosity η scales with $\tau_s/\dot{\gamma}$. In this case, the shear stress τ_s is directly proportional to the shear strain rate $\dot{\gamma}$ (cf. Equation 17.18 with $\sigma \approx 2\tau_s$ and $\dot{\varepsilon} \approx 2\dot{\gamma}$ for a fracture angle of 42°, according to the well-known Schmid's law) and η depends only on temperature. Thus, τ_s shows a similar temperature dependence as the viscosity (compare Figures 17.12 and 17.22).

In Figure 17.22, T_x represents the crystallization temperature, which would need to be shifted significantly closer to the liquidus temperature, if the good glass-forming ability of today's bulk metallic glasses were considered. With the onset of crystallization the rheology of the undercooled liquid changes drastically, leading first to a decrease and, after a critical volume fraction of crystals has nucleated and grown, to an increase in viscosity, η^* (see Figure 17.21). Measurements of viscosity in the Newtonian flow regime are used to evaluate the flow behavior in superplastic forming (see Section 17.4.3) and also to explain the good glass-forming ability of some alloys.

At higher strain rates or lower temperatures, non-Newtonian flow has been observed to depend strongly on temperature and strain rate.[143,144] From a microscopic point of view it is still under debate as to

whether this regime can be classified as homogeneous or inhomogeneous flow.[145] Non-Newtonian flow in a compression test is characterized by an overshoot stress, which occurs upon yielding before steady-state flow at lower stress is reached.[146] This overshoot may be understood as a competition between a slower process, namely the structural breakdown governed by Newtonian flow, and a shear relaxation mechanism governing the steady-state viscosity.[146]

It has also been shown that the transition between Newtonian and non-Newtonian is rather abrupt and can be quantified by the Deborah number, $D_e = \dot{\gamma}\tau$, where $\dot{\gamma}$ is the shear strain rate and τ the relaxation time for the annihilation of the flow defects. A value of $D_e \sim 0.5$ has been measured for amorphous $Pd_{40}Ni_{40}P_{20}$, compared to the typical value of $D_e \sim 1$ known for the onset of flow instability.[145]

17.5.3 Mechanical Properties at Ambient Temperatures

At low temperatures where inhomogeneous deformation prevails, metallic glasses show consistently higher strength than crystalline materials of the same density.[12] This is shown in Figure 17.23, where the average strength of the crystalline and amorphous metals is plotted as a function of their density. Amorphous alloys generally show an average strength that is more than twice that of crystalline alloys. In addition, a linear fit to the data results in an average specific strength of 346 MPa/g/cm^3 for amorphous alloys and 155 MPa/g/cm^3 for crystalline alloys.

The high strength of metallic glasses results in an elastic strain limit of ~2%, which is approximately three to four times higher than that of their crystalline counterparts. Figure 17.24 summarizes data from various references on the yield strength, σ_y, and the Vickers hardness as a function of the Young's modulus, E, for bulk metallic glasses and crystalline metallic alloys.[10] For the same Young's modulus, a strength is reached in bulk metallic glasses that is about three times higher than that of their crystalline counterparts. It is also interesting to note that the metallic glasses show a linear dependence of the yield strength (basically following Hooke's law, $\sigma_y = E\varepsilon$, where ε is the strain) and hardness on the Young's modulus, while the crystalline metals deviate from this linear behavior. This reflects the strong dependency of the deformation behavior in crystalline metals on chemical and therefore microstructural change, which is less pronounced in amorphous materials.

17.5.4 Inhomogeneous Deformation

This section presents typical characteristics of the inhomogeneous flow of metallic glasses. These are important in understanding the general differences in deformation behavior (and their underlying

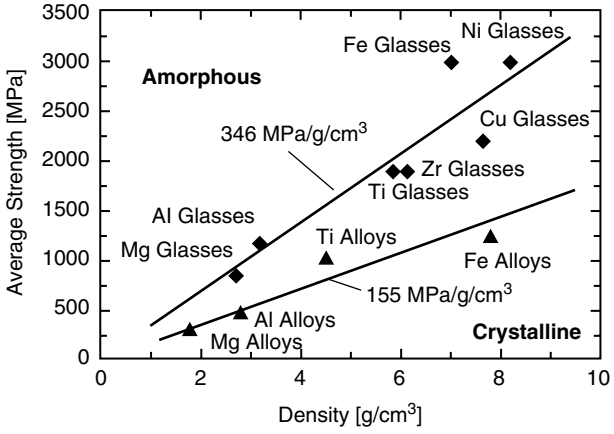

FIGURE 17.23 Average yield strength as a function of density for amorphous and crystalline alloys. (Reproduced from Löffler, J.F., *Z. Metallkd.* 97, 225, 2006. With permission.)

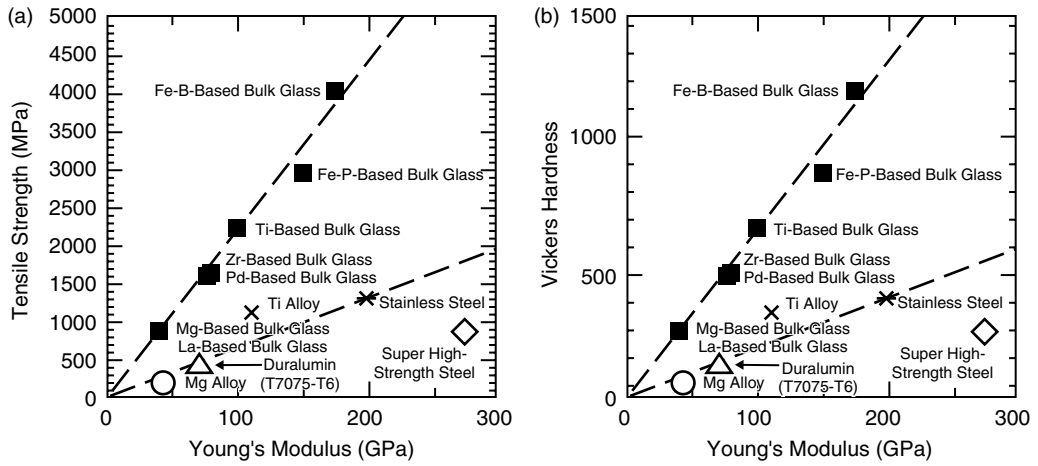

FIGURE 17.24 (a) Tensile strength and (b) Vickers hardness vs. Young's modulus for various amorphous and crystalline materials. (Reproduced from Inoue, A., *Acta Mater.* 48, 279, 2000. With permission.)

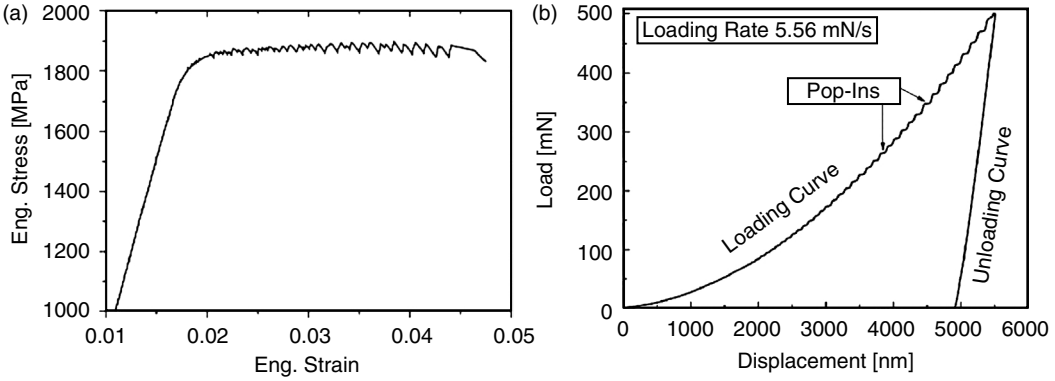

FIGURE 17.25 (a) Compression and (b) nanoindentation tests on glassy $Zr_{52.5}Ti_5Cu_{17.9}Ni_{14.6}Al_{10}$ (Vit105).

mechanisms) compared to those of their crystalline counterparts. The most obvious property observed during deformation is serrated flow (Section 17.5.4.1) and its manifestation in the form of "vein" patterns on fracture surfaces (Section 17.5.4.2). Other important parameters discussed are fracture toughness (Section 17.5.4.3) and plastic strain limits, measured in compression and tension (Section 17.5.4.4).

17.5.4.1 Serrated Flow

In Figure 17.25, a typical stress–strain curve tested in compression (a) and a nanoindentation curve (b) are shown for a Zr-based bulk metallic glass. Both types of curves exhibit nonuniform inhomogeneous deformation, represented by the serrated flow curves in the compression test (a) and the "pop-ins" in the indentation depth signal (b). These discrete steps correspond to single deformation bursts along preexisting or newly formed shear bands.

Within these highly localized shear bands, great shear displacements on the order of a few micrometers can take place and occur within short time intervals of tens to hundreds of milliseconds, depending on the deformation temperature and speed. Therefore, within such shear bands shear strains of greater than 1 have to be assumed. According to the deformation models of References 141 and 147, vacancy-like free volume is shuffled around and underlies a competing process of creation and annihilation of extra free volume. Due to the higher rate of free volume creation, this leads to a softening of the material within a shear band. Whether this deformation before failure is additionally triggered by a local change in the

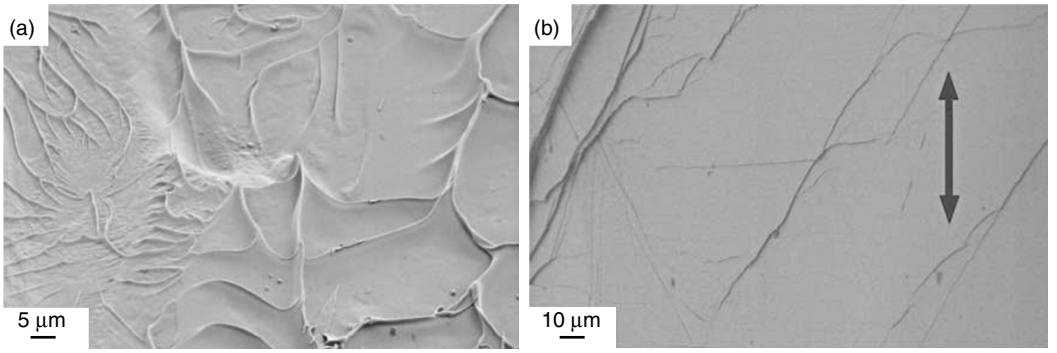

FIGURE 17.26 (a) Fracture surface and (b) shear-band offsets on the surface of a compression specimen of a Zr-based bulk metallic glass.

rheological behavior of the material, that is, a drastic drop in viscosity due to adiabatic heating, is a matter of current research.[148–150]

17.5.4.2 Fracture Surfaces and Shear Bands

Figure 17.26a shows a fracture surface of a Zr-based bulk metallic glass sample tested in compression. It shows a typical vein pattern arising from viscous flow, which occurs during the sudden relief of stress energy at failure and its conversion into heat. Re-solidified droplets are also found frequently, implying that temperatures are sufficiently high at fracture for local melting of the material to occur.

On the surrounding surfaces of compression specimens, shear bands appear as sharp, irregular sub-micrometer wide offsets from the surface, as shown in Figure 17.26b. They are generally oriented in a conjugated configuration, at an angle of ~40 to 45° to the compression direction. This angular dependency of shear bands reflects the stress states in the solid and its associated yield (Mohr–Coulomb) criterion.[151] Note that as shear bands are the main carriers of plastic deformation in metallic glasses, their density is a linear function of the amount of global plastic deformation the material will support before failure.

17.5.4.3 Fracture Toughness

Apart from the high strength and elastic limit observed in bulk metallic glasses, information on fracture toughness (K_c) is crucial for the successful deployment of bulk metallic glasses in structural and functional applications. Fracture toughness is the ability of a material with a preset flaw to withstand an applied load without immediate fracture. Materials exhibiting high fracture toughness generally show ductile fracture, whereas low fracture toughness values are indicative of brittle materials. The fracture toughness is defined as

$$K_c = \sqrt{EG_c} = \bar{c}\sigma_c\sqrt{\pi\, a} \tag{17.20}$$

where E is the Young's modulus and G is the critical strain energy release rate, with subscript c indicating the crucial point at fracture; σ is the stress on the workpiece, a is the notch length and $\bar{c}$ is a correction factor of ~1.1.[152]

As shown above in Figure 17.26b, bulk metallic glasses deform in shear bands and can exhibit very high plastic strains locally. This observation, combined with the fact that bulk metallic glasses exhibit an unusually high fraction of theoretical strength, generally leads to high fracture toughness ($K_c > 20$ MPa $\sqrt{\text{m}}$).[153] However, on a macroscopic level the material cannot be properly termed as ductile and should instead be defined as malleable, that is, with limited plastic strain only in the compressive or bending mode. The K_c values of various bulk metallic glasses are presented in Table 17.3.

Compared to silica glasses, metallic glasses generally show significantly higher fracture toughness. However, they span a large range in K_c because of their intrinsic and extrinsic embrittlement, that is, their

TABLE 17.3 Fracture Toughness Values of Various Metallic Glasses

Material	K_c-values [MPa $\sqrt{m}$]	Ref.
Fused silica	0.5	157
Window glass	0.2	157
$Mg_{65}Cu_{25}Tb_{10}$	2	158
$Cu_{60}Zr_{20}Hf_{10}Ti_{10}$	68	159
$Ti_{50}Ni_{24}Cu_{20}B_1Si_2Sn_3$	50	160
$Zr_{57}Ti_5Cu_{20}Ni_8Al_{10}$	80	161
$Zr_{55}Al_{10}Ni_5Cu_{30}$	67	8
$Zr_{41.2}Ti_{13.8}Cu_{12.5}Ni_{10}Be_{22.5}$	16–86	162–164
$Fe_{40}Ni_{40}P_{14}B_6$	38–48	165
$Ni_{43}Fe_{29}P_{14}Al_3B_6$	120	166
$Pt_{57.5}Cu_{14.7}Ni_{5.3}P_{22.5}$	79–84	167
$Ce_{60}Al_{20}Ni_{10}Cu_{10}$	10	158
$La_{55}Al_{25}Ni_5Cu_{10}Co_5$	5	168

high sensitivity to flaws.[154] In the best cases, where external flaws are suppressed, the fracture toughness reaches values close to those of conventional structural crystalline materials, such as crystalline Al alloys ($\sim$20 to 40 MPa$\sqrt{m}$), steels ($\sim$50 MPa $\sqrt{m}$),[153] Ti alloys (44 to 66 MPa $\sqrt{m}$)[155], and Ni alloys $\sim$(5 to 30 MPa $\sqrt{m}$).[156] Upon aging at sufficiently high temperatures, however, the fracture toughness of metallic glasses decreases significantly,[153] limiting the application of these materials to environments where temperature fluctuations are low. At temperatures where crystallization occurs, fracture toughness may even drop to values as low as 1 MPa $\sqrt{m}$.[163]

17.5.4.4 Ductility and Malleability in Metallic Glasses

Several strategies have been employed to improve the intrinsic and extrinsic effects on the flow behavior of metallic glasses with respect to their fracture toughness and overall plastic strain in compression (malleability):

1. Similar to crystalline metals,[169–171] embrittlement in metallic glasses is strongly related to the elastic properties of the main component of the alloy and is favored by a high ratio of G/B, where G is the elastic shear modulus and B the bulk modulus, or low Poisson's ratio ν.[153,172] Fracture toughness tests and compression tests on various metallic glasses have shown an increase in fracture energy and plastic strain in compression with decreasing G/B and increasing ν. Since ν is generally only high for costly noble metals, applications of such systems may, however, be restricted.[153,167]
2. Another important aspect in choosing the main component is the relaxation behavior of the material as a function of its homologous glass transition temperature. Relaxation in an amorphous structure is generally linked to a topological rearrangement of atoms towards a denser atomic configuration,[173,174] which generates embrittlement due to a reduction of free volume. Metallic glasses with very low glass transition temperatures with respect to the ambient temperature (as with most Mg-based metallic glasses) show room temperature embrittlement after a short period of aging.[56] Therefore, unless relaxation processes can be suppressed by means other than temperature, applications will concentrate mainly on systems where the main components show high glass transition temperatures.
3. A third strategy for improving malleability involves mixing the brittle metallic glass with a more ductile second phase that either acts as an active carrier of plastic strain or passively enhances the multiplication of shear bands via shear-band splitting. This approach will be outlined in greater detail in Sections 17.6.1 and 17.6.2.

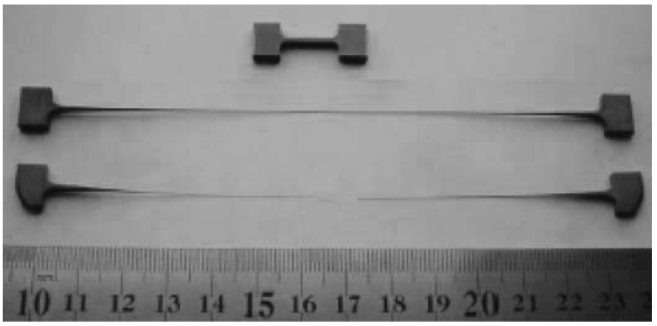

FIGURE 17.27 Tensile specimens of $Zr_{41.25}Ti_{13.75}Ni_{10}Cu_{12.5}Be_{22.5}$ deformed at 616 K. (Reproduced from Wang, G., Shen, J., Sun, J.F., Lu, Z.P., Stachurski, Z.H., and Zhou, B.D., *Intermetallics* 13, 642, 2005. With permission.)

17.5.5 Homogeneous Deformation at Elevated Temperatures

The mechanical behavior of bulk metallic glasses is very sensitive to a change in temperature close to the glass transition temperature. As discussed above, at temperatures far smaller than the glass transition, deformation is inhomogeneous and locally restricted to plastic deformation of a few shear bands, leading to only a few percent of plastic strain (in compression). At temperatures close to T_g, the deformation mechanism changes and becomes homogeneous, this being characterized by an evenly distributed strain over the whole volume. In this case, low flow stresses and large strains up to several hundred percentages can be achieved in tension and compression. At low strain rates the deformation can be described by Newtonian flow, where the viscosity η solely depends on temperature. At higher strain rates the behavior of metallic glasses becomes non-Newtonian and the viscosity depends on both temperature and strain rate[175] (see Section 17.5.2). As seen in Figure 17.27, superplastic flow with several hundred percent strain can be achieved in tension at strain rates of up to 10^{-1} per s at temperatures near T_g.[176,177] This unique behavior of metallic glasses close to the glass transition temperature, where a temperature change triggers a drastic change in strength and ductility, allows processing of the material in the undercooled liquid region to net-shaped parts that exhibit high strength and hardness (see Section 17.4).

17.6 Metallic Glass Composites

As outlined in Section 17.5.4.4, the ductility or malleability of metallic glasses may be greatly increased by introducing a second, more ductile phase into the metallic glass matrix. This section discusses several such processing routines and describes the resulting microstructure and mechanical properties.

17.6.1 *In Situ* Composites

In situ composite formation of a microstructure exhibiting a ductile crystalline phase and a hard metallic glass phase is based on the thermophysical properties of the undercooled melt, its composition, and the nucleation rate of the crystalline phase. The main requirement in such a process is to find a multicomponent composition that (1) leads upon cooling from the melt to the nucleation of a ductile crystalline phase (preferably not an intermetallic phase) of a certain volume percentage, and (2) causes the depletion of the remaining melt by the solidified elements in the direction of a composition that exhibits good glass-forming ability.[178,179] The processing methods (copper mold casting and injection molding) for the production of such composites do not differ from those producing monolithic metallic glasses, but may be altered slightly so that slower cooling rates allow crystallization. For the Zr–Ti–Cu–Ni–Be–Nb system a composition of this type has been found that upon cooling from the melt shows a microstructure of crystalline Ti–Zr–Nb (β) dendrites of bcc structure embedded in a Zr–Ti–Nb–Cu–Ni–Be glassy matrix (Figure 17.28).[178] This composite exhibits enhanced plastic strain under compression. Plastic strain of a

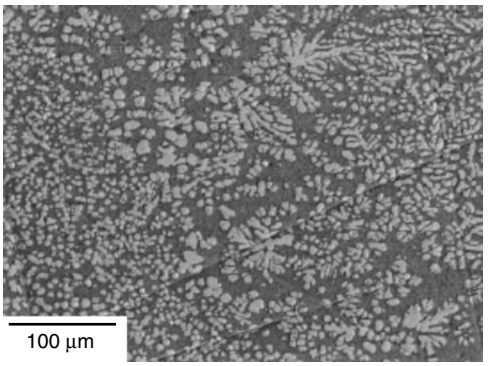

FIGURE 17.28 Dendritic structure of bcc Ti–Zr–Nb β phase (bright) embedded in a glassy Zr–Ti–Nb–Cu–Ni–Be matrix. (Reproduced from Hays, C.C., Kim, C.P., and Johnson, W.L., *Phys. Rev. Lett.* 84, 2901, 2000. With permission.)

low percentage was also seen in tension for this composite[178] when the percentage of the ductile phase was higher than a critical value of ~20 to 30 vol.%. This tensile ductility is important for structural applications.

Such microstructures, composed of dendritic ductile and amorphous tough phases, have meanwhile led to a drastic increase in compressive plastic strain without a significant loss in strength for several other metallic glass systems.[180–182] Compression tests performed on Ti-based bulk metallic glasses containing 20 vol.% of β-Ti(Ta,Sn) dendrites embedded in a nanocrystalline matrix revealed a plastic compressive strain of 15% and a maximum strength of 2.4 GPa. Strain-hardening behavior attributed to the crystalline phase has also been observed, raising expectations of achieving enhanced plastic strain in tension.[181] Similar enhanced mechanical strength and ductility have been observed in as-cast Cu–Zr samples with an equated, nanosized grain structure embedded in an amorphous matrix.[183]

17.6.2 *Ex Situ* Composites

A different approach to forming a composite material was guided by classical particle reinforcement methods, where — as opposed to crystalline solids — particles are meant to represent the phase which enhances plasticity and not increasing strength. Such composites are generally formed by adding solid particles to the liquid melt, forming a metallic glass matrix.[184] The addition of up to 20 vol.% of SiC, W, WC, or Ta particles with sizes ranging between 10 and 40 μm to a Zr-based glassy matrix has been shown to increase the plastic strain by up to 5% without reducing strength compared to the monolithic samples.[185] Much higher plastic strain of up to 18.5% has recently been achieved by adding soft graphite particles of 25 to 75 μm in size to Zr-based metallic glasses.[186] In Figure 17.29 the compression curves for monolithic Vit105 ($Zr_{52.5}Ti_5Cu_{17.9}Ni_{14.6}Al_{10}$) and the alloy reinforced with 3.5 vol.% graphite particles are shown, together with a scanning electron microscopy image of shear-band interaction with the graphite particles.

In contrast to the technique presented in Section 17.6.1, where a ductile phase is formed *in situ* during cooling from the melt, more control, and therefore reproducibility, over the type, size, and volume fraction of the ductile phase can be obtained in foreign-particle-reinforced bulk metallic glasses. Thus the approach presented in Reference 186 is of particular importance for the use of bulk metallic glasses as structural engineering material.

17.6.3 Amorphous Metallic Foams

A different approach to increasing plastic deformation has been explored by introducing a substantial volume fraction of micrometer-sized pores into the material.[187–189] Due to their reduced density such microstructures exhibit a substantial increase in strength vs. density combined with excellent malleability in compression. Metallic foam structures are used nowadays in several structural applications and are also attractive for bone replacements, due to their tunable elastic modulus (dependent on the pore volume[190]).

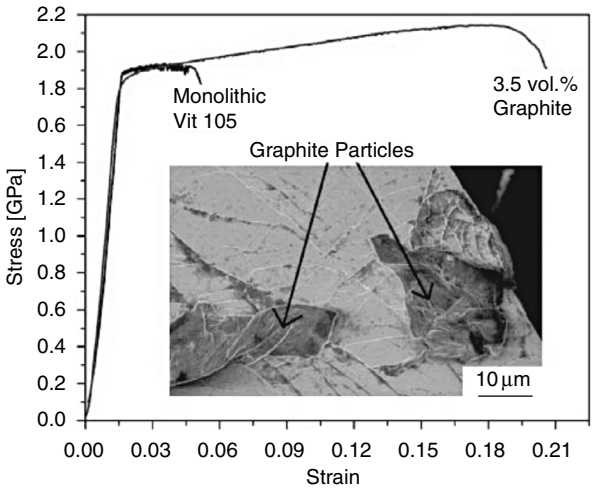

FIGURE 17.29 Compressive stress–strain curves for monolithic Vit105 and Vit105 reinforced with 3.5 vol.% graphite. Inset: Scanning electron microscopy image illustrating shear-band interactions with the graphite particles.

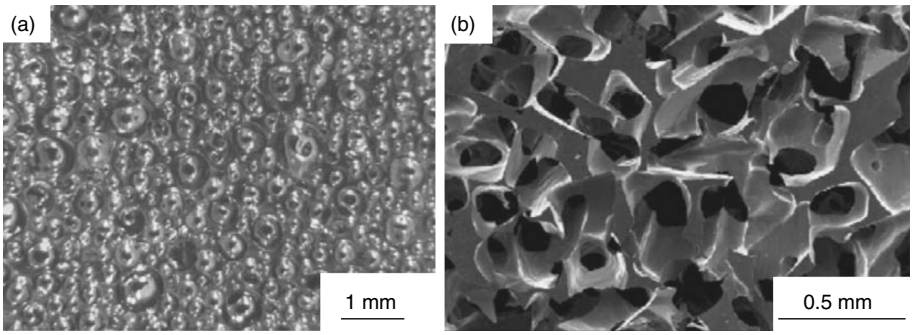

FIGURE 17.30 Metallic glass foams produced via (a) melting of a mixture of Pd-based alloy granulate with hydrated B_2O_3 and subsequent quenching during dehydration of B_2O_3 leading to a closed porosity, and (b) salt replication process (using Zr-based Vit106) leading to an open porosity structure. (Reproduced from Schroers, J., Veazey, C., and Johnson, W.L., *Appl. Phys. Lett.* 82, 370, 2003 and Brothers, A.H. and Dunand, D.C., *Acta Mater.* 53, 4427, 2005. With permission.)

To date several methods have been exploited and applied to metallic glasses, leading either to (1) a closed porosity[187,188] or to (2) an open-cell structure.[189]

Commercially available crystalline foams with a closed porosity are frequently produced by introducing a pressurized gas into the molten state of the metal.[190] A different approach to achieving a closed pore structure has been demonstrated for Pd-based metallic glass foams, where the alloy powder is mixed with hydrated B_2O_3. The latter releases gas at elevated temperatures and leads to an expansion of the molten metal volume via uniformly distributed gas bubbles[187] (Figure 17.30a). Yet another method takes advantage of the stability of the metallic glass in the undercooled liquid region, where within this temperature range gas bubbles preintroduced during the melting process expand to their final size.[188]

Open porous structures for metals are typically produced by a salt replication process, which has produced aluminum foams routinely since the 1960s.[190] This technique has now been successfully applied to Vit106 ($Zr_{57}Nb_5Cu_{15.4}Ni_{12.6}Al_{10}$), where compressive strains of 60% were reached in samples with a pore volume of 14 to 28 vol.%.[191]

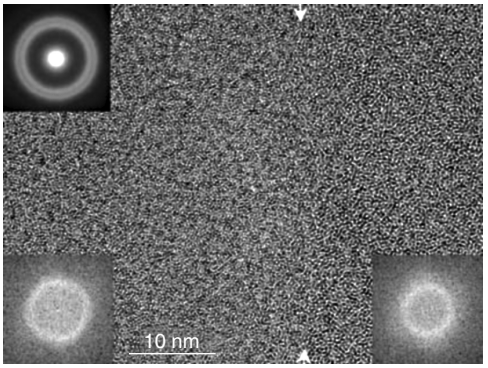

FIGURE 17.31 HR-TEM image of the alloy $La_{27.5}Zr_{27.5}Cu_{10}Ni_{10}Al_{25}$ at the interface of a Zr-rich phase (on the left) and a La-rich phase (on the right). Fast Fourier-transformed images are shown for the left area (lower left-hand image, larger ring) and for the right area (lower right-hand image, smaller ring). The selected-area electron diffraction pattern (upper left-hand corner) shows two distinct rings. (Reproduced from Kündig, A.A., Ohnuma, M., Ping, D.H., Ohkubo, T., and Hono, K., *Acta Mater.* 52, 2441, 2004. With permission.)

17.6.4 Two-Phase Metallic Glasses

A recent approach to *in situ*-formed metallic glass composites are alloys that decompose in the liquid phase into two compositions both of which form a metallic glass, as in the systems La–Zr–Cu–Ni–Al,[192] Y–Ti–Al–Co,[193] and Ni–Nb–Y.[194] In the case of $La_{27.5}Zr_{27.5}Cu_{10}Ni_{10}Al_{25}$, the alloy separates into a La–Cu-rich and a Zr–Ni-rich phase, both compositions being close to bulk glass-formers. The interface is rather sharp and can be detected by HR-TEM due to a larger average atomic distance in the La-rich alloy, as seen in Figure 17.31.

As with crystalline/amorphous composites, the abrupt change in composition can halt, deflect, or multiply shear bands. In a bulk metallic glass of the Cu–Zr–Al–Ag system the separation into Cu-rich and Al-rich phases has been shown to exhibit enhanced malleability and strength compared to monolithic single-phase amorphous metals.[195] Similarly, a high plastic strain of $>16\%$ and a flow stress of 2 GPa has recently been reported for a $Cu_{47.5}Zr_{47.5}Al_5$ bulk metallic glass separating into two immiscible amorphous phases.[183]

17.7 Applications

Metallic glasses exhibit outstanding mechanical, magnetic, and chemical properties, and possess forming capabilities suitable for a large range of applications — of which only a small fraction have so far been commercially deployed. For successful commercialization a careful comparison of the advantages of a metallic glass product and its higher price is necessary. The cost of metallic glasses is determined by (1) the raw material costs and (2) the processing costs involved. For current bulk metallic glasses, very clean (and therefore expensive) raw materials are required that must be processed under clean (and likewise expensive) conditions. For applications where thin layers or ribbons of metallic glass suffice, a larger range of compositions may be applied and purity is less important. For this reason metallic glass ribbons for magnetic applications are currently their most important application industrially, followed by metallic glass coatings for corrosion protection and then bulk metallic glasses for structural applications. Metallic glass ribbons can be produced inexpensively as the raw materials may be similar in grade to the same elements (e.g. Fe, Ni, Co, Si and B) used in the high-volume steel industry. Thanks to the increase in glass-forming ability brought about by alloy development, not only has the maximum thickness of an amorphous part been increased, but also the process stability of parts with dimensions smaller than the maximum casting thickness. Thus the development of good metallic glass-formers is a key factor for the deployment of metallic glasses on an industrial scale.

17.7.1 Magnetic Metallic Glass Ribbons

Metallic glasses containing large amounts of ferromagnetic material often demonstrate superior soft-magnetic behavior and high permeability. For applications in transformer cores, metallic glasses such as Metglas® Alloy 2605SA1 can reduce transformation losses by 70% compared to (crystalline) iron cores, which clearly justifies their higher production cost.[196]

Also successful has been the deployment of a combination of metallic glass ribbons in article surveillance systems. The marker in this system consists of a ferromagnetic metallic glass ribbon (e.g. $Fe_{40}Ni_{38}Mo_4B_{18}$) which shows magnetostrictive behavior at a certain bias field. The ribbon is magnetically biased with another ribbon of a hard magnetic material, typically of an annealed metallic glass. If the marker is excited in an electromagnetic field at the correct frequency (e.g. 60 kHz), the magnetostrictive ribbon will vibrate mechanically and emit an electromagnetic RF signal of the same frequency as the activation, which decays exponentially with time. The marker is activated by a pulse from an electromagnetic field, placed for example at the exit of a retail shop, and the response is measured by a receiver coil. After demagnetizing the hard magnetic ribbon, the magnetostrictive behavior of the soft magnetic ribbon ceases to be activated by the RF coil.[197]

One potential future application of magnetic metallic glasses may lie in the area of shielding alternating magnetic fields from power lines. Efficient shielding is obtained, for example, by using two layers of the alloy $Fe_{67}Co_{18}B_{14}Si_1$ (Metglas 2605CO), which possesses good shielding ability of large fields.[196] Magnetic glasses lacking metalloids[198] may also be interesting for such applications.

17.7.2 Metallic Glass Coatings

A large variety of coating and deposition techniques, such as physical and chemical vapor deposition, are currently deployed commercially. Thermal spray coating in particular has become one of the most successful techniques for producing large-scale amorphous metal coatings for industrial applications.[199] Here the coating material is introduced as a wire, molted by a combustion or plasma torch far above the melting temperature, and sprayed via a noble gas jet as small droplets onto a substrate kept at room temperature. The droplets are a few hundred micrometers in size and arrive at the substrate at a velocity of several hundred meters per second. The hot droplets melt a thin layer of the surface, weld onto it, and are quenched at a high cooling rate (10^4 to 10^6 K/s). With the high cooling rates given, a large range of alloy compositions may be quenched into a glass and optimized for corrosion and mechanical properties, while the substrate properties remain unaffected and can be chosen independently.

Metallic glasses based on, for example, Fe, Ni, and Co show very good corrosion resistance and high strength compared to their crystalline counterparts. Their high corrosion resistance stems mainly from their composition (i.e., substantial Si and B contents) and chemical homogeneity. The absence of grain boundaries generates uniform protective oxide layers. Applications range from fireboxes for large boilers (1500 MW) to refinery cookers.[199] One project that may also lead to large-volume application of metallic glasses is the study of coating materials for radioactive waste containers, with special attention to long-term corrosion resistance.[200]

For wear resistance, again only a thin layer is needed, and the coating material can be optimized for mechanical strength (i.e., hardness), while the substrate material exhibits greater toughness. Due to similar base elements in the steel substrate and the amorphous coating, adhesion is usually very good.

Metallic glass ribbons and coatings can also be used as catalytic materials. In many cases the activity of the amorphous phase is greater than that of its crystalline counterpart. For example, the turnover frequency for semihydrogenation of a propargylic alcohol in "supercritical" carbon dioxide is 50 times higher on an amorphous Pd–Si catalyst than on conventional supported Pd on SiO_2.[201]

17.7.3 Bulk Metallic Glasses

Structural applications of fully bulk amorphous parts continue to gain momentum. The first applications of these materials were as golf club heads, tennis racket elements, and baseball bats, all benefiting from the

excellent elastic properties of metallic glasses.[199] The development of processing equipment has accompanied new applications, and processing in the undercooled liquid region ("injection casting") has been studied and exploited. This procedure is more stable to crystallization (see Section 17.3.3) than heating the glass from room temperature ("superplastic forming"), but both processes present the advantage of very low solidification shrinkage and the potential for near-net-shape forming of parts (see Section 17.4.2 and Section 17.4.3). The resulting applications include electronic casings and hinges[199] (see, e.g., Figure 17.18). A low processing temperature in combination with high material strength is also a property unique to metallic glasses. High-strength parts can now be processed similarly to plastics (see, e.g., Figure 17.20).

Another advantage of metallic glasses is their combination of high yield strength and low Young's modulus; this has inspired applications such as a Coriolis force flow meter[202] and pressure sensor membranes.[203] As mentioned above, the improved processability of bulk metallic glasses also makes them attractive for applications where only thin parts are needed.

17.7.4 Micro- and Nano-Patterned Structures

Due to the absence of grain boundaries, metallic glasses are mechanically and chemically homogenous on all length scales down to a few nanometers. This makes glasses (and single crystals such as Si) preferred materials for micro- and nanostructured parts. Prototypes of microgears, in which high precision and a low abrasion rate are important, have been tested successfully.[204] Structures with dimensions down to the nanometer range such as test grooves and compact disc templates have been directly patterned[205] and replicated from Si wafers[130,135] with high precision (see Figure 17.17). These high-strength, high-precision structures can be used, for example, for the embossing of polymers, which can then be used in microfluidics or, if the structures are selectively filled with metals, in microelectronics.

17.7.5 Medical Applications

Deploying metallic glasses in surgical instruments (scissors, etc.) or as implant material takes advantage of their unique combination of low Young's modulus, high strength, high elastic limit, and good corrosion resistance. Zr-based metallic glasses form stable oxide layers and the release of alloy elements from a Zr-based implant is low. Excluding the toxic elements Ni and Cu will increase biocompatibility still further; a Ni-free, Zr-based metallic glass with a low critical cooling rate has recently been developed

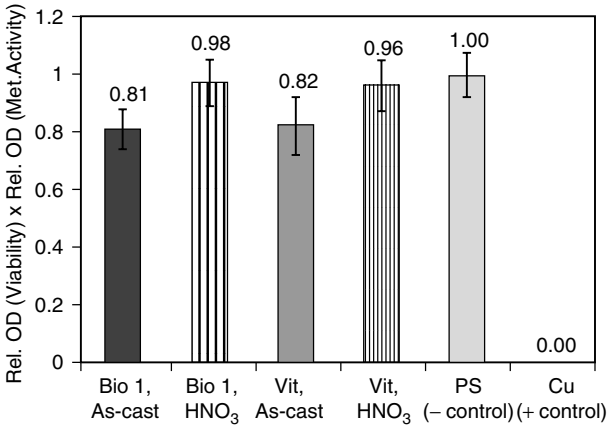

FIGURE 17.32 Direct cytotoxicity tests (performed by measuring the viability and metabolic activity of mouse fibroblasts via optical density measurements) on $Zr_{58}Cu_{22}Fe_8Al_{12}$ (Bio 1) and $Zr_{58.5}Cu_{15.6}Ni_{12.8}Al_{10.3}Nb_{2.8}$ (Vit106a) in the as-cast state and after surface treatment in nitric acid, in comparison to negative (PS, polystyrene) and positive (Cu) controls. (Reproduced from Buzzi, S., Jin, K., Uggowitzer, P.J., Tosatti, S., Gerber, I., and Löffler, J.F., *Intermetallics*, 14, 729, 2006. With permission.)

for this purpose.[206] Cytotoxicity measurements of the latter, $Zr_{58}Cu_{22}Fe_8Al_{12}$, and a Ni-bearing metallic glass, $Zr_{58.5}Cu_{15.6}Ni_{12.8}Al_{10.3}Nb_{2.8}$ (Vit 106a), show good biocompatibility for both alloys, which can be increased to the level of polystyrene (the negative control) after a passivation treatment in HNO_3[207] (see Figure 17.32). Bone plates and aneurism stents may be among the applications that result.

Acknowledgments

This work was supported by the Swiss National Science Foundation (Grant # 200021-105647 and Grant # 200021-108071), by an ETH Research Grant (Grant # TH-21/04-2), and by start-up funds from ETH Zurich (J.F.L.).

References

[1] Buckel, W. and Hilsch, R., Supraleitung und Widerstand von Zinn mit Gitterstörungen (Mitteilungen zur Supraleitung II). *Z. Phys.* 131, 420, 1952.
[2] Klement, W., Willens, R.H., and Duwez, P., Non-crystalline structure in solidified gold-silicon alloys. *Nature* 187, 869, 1960.
[3] Duwez, P., Structure and properties of alloys rapidly quenched from the liquid state. *ASM Trans. Quart.* 60, 607, 1967.
[4] Cahn, R.W., Metallic glasses. *Contemp. Phys.* 21, 43, 1980.
[5] Turnbull, D., Metastable structures in metallurgy. *Metall. Trans. A* 12, 695, 1981.
[6] Johnson, W.L., Metallic glasses. *Metals Handbook* 2, 805, 1990.
[7] Johnson, W.L., Metastable phases (Chap. 29), in *Intermetallic Compounds: Vol. 1, Principles*, J.H. Westbrook and R.L. Fleischer (Eds.), John Wiley & Sons Ltd., Chichester, 1994, p. 687.
[8] Inoue, A., *Bulk Amorphous Alloys, Preparation and Fundamental Characteristics.* Trans. Tech. Publ., Switzerland, 1998.
[9] Johnson, W.L., Bulk glass-forming metallic alloys: Science and technology. *MRS Bull.* 24, 42, 1999.
[10] Inoue, A., Stabilization of metallic supercooled liquid and bulk amorphous alloys. *Acta Mater.* 48, 279, 2000.
[11] Löffler, J.F., Bulk metallic glasses. *Intermetallics* 11, 529, 2003; reprinted from J. F. Löffler, in *The Encyclopedia of Materials: Science and Technology*, K.H.J. Buschow, R.W. Cahn, M.C. Flemings, B. Ilschner, E.J. Kramer, and S. Mahajan (Eds.), Pergamon/Elsevier Science, Amsterdam, 2003.
[12] Löffler, J.F., Recent progress in the area of bulk metallic glasses. *Z. Metallkd.* 97, 225, 2006.
[13] Schwarz, R.B. and Johnson, W.L., Formation of an amorphous alloy by solid-state reaction of the pure polycrystalline metals. *Phys. Rev. Lett.* 51, 415, 1983.
[14] Russell, K.C., Phase stability under irradiation. *Prog. Mater. Sci.* 28, 229, 1984.
[15] Ponyatovsky, E.G. and Barkalov, O.I., Pressure-induced amorphous phases. *Mater. Sci. Eng. Rep.* 8, 147, 1992.
[16] Schultz, L. and Eckert, J., Mechanically alloyed glassy metals. *Topics Appl. Phys.* 72, 69, 1994.
[17] Valiev, R.Z., Islamgaliev, R.K., and Alexandrov, I.V., Bulk nanostructured materials from severe plastic deformation. *Prog. Mater. Sci.* 45, 103, 2000.
[18] Duwez, P., Willens, R.H., and Klement Jr., W., Continuous series of metastable solid solutions in silver-copper alloys. *J. Appl. Phys.* 31, 1136, 1960.
[19] Duwez, P., Metallic glasses-historical background (Chap. 2), in *Glassy Metals I (Topics in Applied Physics, Vol. 46),* H.J. Güntherodt and H. Beck (Eds.), Springer, Berlin, 1981, p. 19.
[20] Jones, H., Splat cooling and metastable phases. *Rep. Prog. Phys.* 36, 1425, 1973.
[21] Chen, H.S. and Turnbull, D., Formation, stability and structure of palladium-silicon based alloy glasses. *Acta Metall.* 17, 1021, 1969.
[22] Gibbs, J.H. and DiMarzio, E.A., Nature of the glass transition and the glassy state. *J. Chem. Phys.* 28, 373, 1958.

[23] Cohen, M.H. and Turnbull, D., Molecular transport in liquids and glasses. *J. Chem. Phys.* 31, 1164, 1959.
[24] Cohen, M.H. and Turnbull, D., Composition requirements for glass formation in metallic and ionic systems. *Nature* 189, 131, 1961.
[25] Turnbull, D., Under what conditions can a glass be formed? *Contemp. Phys.* 10, 473, 1969.
[26] Smith, C.H., Applications of rapidly solidified soft magnetic alloys (Chap. 19), in *Rapidly Solidified Alloys: Processes, Structure, Properties, Applications*, H.H. Liebermann (Ed.), Dekker Inc., New York, 1993, p. 617.
[27] Liebermann, H.H. and Graham Jr., C.D., Production of amorphous alloy ribbons and effects of apparatus parameters on ribbon dimensions. *IEEE Trans. Mag.* 12, 921, 1976.
[28] Chen, H.S., Thermodynamic considerations on the formation and stability of metallic glasses. *Acta Metall.* 22, 1505, 1974.
[29] Lee, M.C, Kendall, J.M., and Johnson, W.L., Spheres of the metallic glass $Au_{55}Pb_{22.5}Sb_{22.5}$ and their surface characteristics. *Appl. Phys. Lett.* 40, 383, 1982.
[30] Drehman, A.L., Greer, A.L., and Turnbull, D., Bulk formation of a metallic glass — $Pd_{40}Ni_{40}P_{20}$. *Appl. Phys. Lett.* 41, 716, 1982.
[31] Kui, H.W., Greer, A.L., and Turnbull, D., Formation of bulk metallic glass by fluxing. *Appl. Phys. Lett.* 45, 615, 1984.
[32] Inoue, A., Zhang, T., and Masumoto, T., Zr–Al–Ni amorphous alloys with high glass-transition temperature and significant supercooled liquid region. *Mater. Trans., JIM* 31, 177, 1990.
[33] Inoue, A. et al., Mg–Cu–Y amorphous alloys with high mechanical strengths produced by a metallic mold casting method. *Mater. Trans., JIM* 32, 609, 1991.
[34] Inoue, A. et al., Bulk La–Al–TM (TM = transition-metal) amorphous alloy with high tensile strength produced by a high-pressure die-casting method. *Mater. Trans., JIM* 34, 351, 1993.
[35] Peker, A. and Johnson, W.L., A highly processable metallic glass — $Zr_{41.2}Ti_{13.8}Cu_{12.5}Ni_{10}Be_{22.5}$. *Appl. Phys. Lett.* 63, 2342, 1993.
[36] Peker, A. and Johnson, W.L., Be bearing amorphous metallic alloys formed at low cooling rates, U.S. Patent No. 5,288,344, 1993.
[37] Lin, X.H. and Johnson, W.L., Formation of Ti–Zr–Cu–Ni bulk metallic glasses. *J. Appl. Phys.* 78, 6514, 1995.
[38] Davies, H.A., Metallic glass formation (Chap. 2), in *Amorphous Metallic Alloys*, F.E. Luborsky (Ed.), Butterworths Monographs in Materials, London, 1983, p. 8.
[39] Bennet, C.H., Serially deposited amorphous aggregates of hard spheres. *J. Appl. Phys.* 43, 2727, 1972.
[40] Rahman, A., Mandell, M.J., and McTague, J.P., Molecular-dynamics study of an amorphous Lennard-Jones system at low-temperature. *J. Chem. Phys.* 64, 1564, 1976.
[41] Kramer, J., Non conductive transformations in metal. *Ann. Phys.* 19, 37, 1934.
[42] Allen, R.P., Dahlgren, S.D., and Merz, M.D., in *Rapidly Quenched Metals II*, N.J. Grant and B.C. Giessen (Eds.), MIT Press, Cambridge, 1976, p. 37.
[43] Granqvist, C.G. and Buhrman, R.A., Ultrafine metal particles. *J. Appl. Phys.* 47, 2200, 1976.
[44] Birringer, R. et al., Nanocrystalline materials — An approach to a novel solid structure with gas-like disorder. *Phys. Lett. A* 102, 365, 1984.
[45] Gleiter, H., Nanocrystalline materials. *Prog. Mater. Sci.* 33, 223, 1989.
[46] Gleiter, H., Nanostructured materials: Basic concepts and microstructure. *Acta Mater.* 48, 1, 2000.
[47] Cahn, R.W., Background to rapidly solidification processes (Chap. 1), in *Rapid Solidified Alloys*, H.H. Liebermann (Ed.), Dekker Inc., New York, 1993, p. 5.
[48] Polk, D., Method of continuous casting metal filament on interior groove of chill roll, U.S. Patent 3,881,542 (1975).
[49] Kavesh, S., Method of forming metallic filament cast on interior surface of inclined annular quench roll, U.S. Patent 3,881,540 (1975).

[50] Pond, R.B. and Maddin, R., A method of producing rapidly solidified filamentary castings. *Trans, Met. Soc. AIME* 245, 2475, 1969.
[51] Ohnaka, I. and Fukusako, T., Production of metallic filament by ejecting molten lead into water or atmosphere and stability of molten lead jet. *J. Japan Inst. Met.* 42, 415, 1978.
[52] Narasimhan, M.C., Continuous casting method for metallic strips, U.S. Patent 4,142,571 (1979).
[53] Anantharaman, T.R. and Suryanarayana, C., *Rapidly Solidified Metals.* Trans. Tech. Publ., Switzerland, 1987.
[54] Löffler, J.F. and Johnson, W.L., Crystallization of Mg–Al and Al-based metallic liquids under ultra-high gravity. *Intermetallics* 10, 1167, 2002.
[55] Löffler, J.F. et al., Eutectic isolation in Mg–Al–Cu–Li(–Y) alloys by centrifugal processing. *Phil. Mag.* 83, 2797, 2003.
[56] Castellero, A. et al., Critical Poisson's ratio for room temperature embrittlement of amorphous $Mg_{85}Cu_5Y_{10}$. *Phil. Mag. Lett.* (in press).
[57] Egami, T., Atomic structure of rapidly solidified alloys (Chap. 9), in *Rapidly Solidified Alloys*, H.H. Liebermann (Ed.), Dekker Inc., New York, 1993, p. 231.
[58] Warren, B.E., *X-ray diffraction.* Dover, New York, 1969.
[59] Wagner, C.N.J., Direct methods for the determination of atomic-scale structure of amorphous solids (x-ray, electron, and neutron scattering). *J. Non-Cryst. Solids* 31, 1, 1978.
[60] Löffler, J.F. and Weissmüller, J., Grain-boundary atomic structure in nanocrystalline palladium from x-ray atomic distribution functions. *Phys. Rev. B* 52, 7076, 1995.
[61] Saida, J., Matsushita, M., and Inoue, A., Direct observation of icosahedral cluster in $Zr_{70}Pd_{30}$ binary glassy alloy. *Appl. Phys. Lett.* 79, 412, 2001.
[62] Saida, J., Matsushita, M., and Inoue, A., Nanoicosahedral quasicrystalline phase in Zr–Pd and Zr–Pt binary alloys. *J. Appl. Phys.* 90, 4717, 2001.
[63] Bernal, J.D., Geometrical approach to the structure of liquids. *Nature* 183, 141, 1959.
[64] Bernal, J.D., Co-ordination of randomly packed spheres. *Nature* 188, 910, 1960.
[65] Scott, G.D., Packing of equal spheres. *Nature* 188, 908, 1960.
[66] Finney, J.L., Random packings and structure of simple liquids. 1. Geometry of random close packing. *Proc. Roy. Soc. London Ser. A-Math. Phys. Sci.* 319, 479, 1970.
[67] Finney, J.L., Random packings and structure of simple liquids. 2. Molecular geometry of simple liquids. *Proc. Roy. Soc. London Ser. A-Math. Phys. Sci.* 319, 495, 1970.
[68] Egami, T., Structural relaxation in amorphous $Fe_{40}Ni_{40}P_{14}B_6$ studied by energy dispersive x-ray diffraction. *J. Mater. Sci.* 13, 2587, 1978.
[69] Srolovitz, D., Egami, T., and Vitek, V., Radial distribution function and structural relaxation in amorphous solids. *Phys. Rev. B* 24, 6936, 1981.
[70] Gaskell, P.H., A new structural model for amorphous transition metal silicides, borides, phosphides and carbides. *J. Non-Cryst. Solids* 32, 207, 1979.
[71] Zallen, R., *The Physics of Amorphous Solids.* Wiley-VCH, Weinheim, 2004.
[72] Polk, D.E., Structural model for amorphous metallic alloys. *Scripta Metall.* 4, 117, 1970.
[73] Inoue, A. et al., High packing density of Zr- and Pd-based bulk amorphous alloys. *Mater. Trans., JIM* 39, 318, 1998.
[74] Wang, W.H. et al., Microstructural transformation in a $Zr_{41}Ti_{14}Cu_{12.5}Ni_{10}Be_{22.5}$ bulk metallic glass under high pressure. *Phys. Rev. B* 62, 11292, 2000.
[75] Egami, T. and Waseda, Y., Atomic size effect on the formability of metallic glasses. *J. Non-Cryst. Solids* 64, 113, 1984.
[76] Zhang, T., Inoue, A., and Masumoto, T., Amorphous Zr–Al–Tm (Tm = Co, Ni, Cu) alloys with significant supercooled liquid region of over 100 K. *Mater. Trans., JIM* 32, 1005, 1991.
[77] Miracle, D.B., Sanders, W.S., and Senkov, O.N., The influence of efficient atomic packing on the constitution of metallic glasses. *Phil. Mag.* 83, 2409, 2003.
[78] Lu, Z.P. and Liu, C.T., Glass formation criterion for various glass-forming systems. *Phys. Rev. Lett.* 91, 115505, 2003.

[79] Inoue A. and Takeuchi, A., Recent progress in bulk glassy alloys. *Mater. Trans. JIM* 43, 1892, 2002.
[80] Inoue, A., Bulk glassy and nonequilibrium crystalline alloys by stabilization of supercooled liquid: fabrication, functional properties and applications (Part 1), *Proc. Jpn. Acad. Ser. B* 81, 156, 2005.
[81] Boudreaux, D.S., Structure of metallic glass alloys (Chap. 1), in *Glassy Metals: Magnetic, Chemical and Structural Properties*, R. Hasegawa (Ed.), CRC Press, Boca Raton, FL, 1983, p. 1.
[82] Eckert, J. et al., Crystallization behavior and phase formation in Zr–Al–Cu–Ni metallic glass containing oxygen. *Mater. Trans., JIM* 39, 623, 1998.
[83] Wanderka, N. et al, Formation of quasicrystals in $Zr_{46.8}Ti_{8.2}Cu_{7.5}Ni_{10}Be_{27.5}$ bulk glass. *Appl. Phys. Lett.* 77, 3935, 2000.
[84] Löffler, J.F. et al., Structural and electronic properties of Zr–Ti–Cu–Ni–Be alloys. *Mat. Res. Soc. Symp. Proc.* 644, L1.9.1, 2001.
[85] Pekarskaya, E., Löffler, J.F., and Johnson, W.L., Microstructural studies of crystallization of a Zr-based bulk metallic glass. *Acta Mater.* 51, 4045, 2003.
[86] Frank, F.C., Supercooling of liquids. *Proc. Roy. Soc. A*, 215, 43, 1952.
[87] Nelson, D.R., Order, frustration, and defects in liquids and glasses. *Phys. Rev. B* 28, 5515, 1983.
[88] Tang, X.P. et al., Devitrification of the $Zr_{41.2}Ti_{13.8}Cu_{12.5}Ni_{10.0}Be_{22.5}$ bulk metallic glass studied by XRD, SANS, and NMR. *J. Non-Cryst. Solids* 317, 118, 2003.
[89] Waniuk, T.A., Schroers, J., and Johnson, W.L., Timescales of crystallization and viscous flow of the bulk glass-forming Zr–Ti–Ni–Cu–Be alloys. *Phys. Rev. B* 67, 184203, 2003.
[90] Holland-Moritz, D., Herlach, D.M., and Urban, K., Observation of the undercoolability of quasicrystal-forming alloys by electromagnetic levitation. *Phys. Rev. Lett.* 71, 1196, 1993.
[91] Glade, S.C. et al., Thermodynamics of $Cu_{47}Ti_{34}Zr_{11}Ni_8$, $Zr_{52.5}Cu_{17.9}Ni_{14.6}Al_{10}Ti_5$ and $Zr_{57}Cu_{15.4}$ $Ni_{12.6}Al_{10}Nb_5$ bulk metallic glass forming alloys. *J. Appl. Phys.* 87, 7242, 2000.
[92] Fan, G.J. et al., Thermodynamics, enthalpy relaxation and fragility of the bulk metallic glass-forming liquid $Pd_{43}Ni_{10}Cu_{27}P_{20}$. *Acta Mater.* 52, 667, 2004.
[93] Lu, I.R. et al., Thermodynamic properties of Pd-based glass-forming alloys. *J. Non-Cryst. Solids* 252, 577, 1999.
[94] Kim, Y.J. et al., Experimental determination of the time–temperature–transformation diagram of the undercooled $Zr_{41.2}Ti_{13.8}Cu_{12.5}Ni_{10.0}Be_{22.5}$ alloy using the containerless electrostatic levitation processing technique. *Appl. Phys. Lett.* 68, 1057, 1996.
[95] Uhlmann, D.R., Glass formation. *J. Non-Cryst. Solids* 25, 42, 1977.
[96] Angell, C.A. and Sichina, W., Thermodynamics of the glass transition: empirical aspects. *Ann. New York Acad. Sci.* 279, 53, 1976.
[97] Angell, C.A., Formation of glasses from liquids and biopolymers. *Science* 267, 1924, 1995.
[98] Busch, R., Bakke, E., and Johnson, W.L., Viscosity of the supercooled liquid and relaxation at the glass transition of the $Zr_{46.75}Ti_{8.25}Cu_{7.5}Ni_{10}Be_{27.5}$ bulk metallic glass forming alloy. *Acta Mater.* 46, 4725, 1998.
[99] Waniuk, T.A. et al., Equilibrium viscosity of the $Zr_{41.2}Ti_{13.8}Cu_{12.5}Ni_{10.0}Be_{22.5}$ bulk metallic glass-forming liquid and viscous flow during relaxation, phase separation, and primary crystallization. *Acta Mater.* 46, 5229, 1998.
[100] Masuhr, A. et al., Time scales for viscous flow, atomic transport, and crystallization in the liquid and supercooled liquid states of $Zr_{41.2}Ti_{13.8}Cu_{12.5}Ni_{10.0}Be_{22.5}$. *Phys. Rev. Lett.* 82, 2290, 1999.
[101] Mukherjee, S., Johnson, W.L., and Rhim, W.K., Noncontact measurement of high-temperature surface tension and viscosity of bulk metallic glass-forming alloys using the drop oscillation technique. *Appl. Phys. Lett.* 86, 014104, 2005.
[102] Johnson, W.L., Physics and metallurgy of bulk glass forming alloys, in *Science of Alloys for the 21st Century: A Hume-Rothery Symposium Celebration,* P.E.A. Turchi, R.D. Shull, and A. Gonis (Eds.), The Minerals, Metals & Materials Society, 2000, p. 183.
[103] Busch, R., Liu, W., and Johnson, W.L., Thermodynamics and kinetics of the $Mg_{65}Cu_{25}Y_{10}$ bulk metallic glass forming liquid. *J. Appl. Phys.* 83, 4134, 1998.

[104] Busch, R., Kim, Y.J., and Johnson, W.L., Thermodynamics and kinetics of the undercooled liquid and the glass transition of the $Zr_{41.2}Ti_{13.8}Cu_{12.5}Ni_{10.0}Be_{22.5}$ alloy. *J. Appl. Phys.* 77, 4039, 1995.

[105] Chen, H.S., A method for evaluating viscosities of metallic glasses from the rates of thermal transformations. *J. Non-Cryst. Solids* 27, 257, 1978.

[106] Marcus, M. and Turnbull, D., On the correlation between glass-forming tendency and liquidus temperature in metallic alloys. *Mater. Sci. Eng.* 23, 211, 1976.

[107] Löffler, J.F., Schroers, J., and Johnson, W.L., Time–temperature–transformation diagram and microstructures of bulk glass forming $Pd_{40}Cu_{30}Ni_{10}P_{20}$. *Appl. Phys. Lett.* 77, 681, 2000.

[108] Rhim, W.K. et al., An electrostatic levitator for high-temperature containerless materials processing in 1-g. *Rev. Sci. Instrum.* 64, 2961, 1993.

[109] Johnson, W.A. and Mehl, R.F., Reaction kinetics in processes of nucleation and growth. *Trans. Am. Inst. Min. Metall. Eng.* 135, 416, 1939.

[110] Avrami, M., Kinetics of phase change III: Granulation, phase change an microstructures. *J. Chem. Phys.* 9, 177, 1941.

[111] Nishiyama, N. and Inoue, A., Supercooling investigation and critical cooling rate for glass formation in Pd–Cu–Ni–P alloy. *Acta Mater.* 47, 1487, 1999.

[112] Schneider, S., Thiyagarajan, P., and Johnson, W.L., Formation of nanocrystals based on decomposition in the amorphous $Zr_{41.2}Ti_{13.8}Cu_{12.5}Ni_{10.0}Be_{22.5}$ alloy. *Appl. Phys. Lett.* 68, 493, 1996.

[113] Löffler, J.F. and Johnson, W.L., Model for decomposition and nanocrystallization of deeply undercooled $Zr_{41.2}Ti_{13.8}Cu_{12.5}Ni_{10}Be_{22.5}$. *Appl. Phys. Lett.* 76, 3394, 2000.

[114] Löffler, J.F. et al., Comparison of the decomposition and crystallization behavior of Zr and Pd based bulk amorphous alloys. *Mater. Sci. Forum* 343, 179, 2000.

[115] Schroers, J. et al., Pronounced asymmetry in the crystallization behavior during constant heating and cooling of a bulk metallic glass-forming liquid. *Phys. Rev. B* 60, 11858, 1999.

[116] Löffler, J.F. et al., Crystallization of bulk amorphous Zr–Ti(Nb)–Cu–Ni–Al. *Appl. Phys. Lett.* 77, 525, 2000.

[117] Kündig, A.A. et al., Influence of decomposition on the thermal stability of undercooled Zr–Ti–Cu–Ni–Al alloys. *Scripta Mater.* 44, 1269, 2001.

[118] Schroers, J., The Superplastic Forming of Bulk Metallic Glasses. *J. Mater. JOM* 57, 35, 2005.

[119] Zhang, B. et al., Amorphous metallic plastic. *Phys. Rev. Lett.* 94, 205502, 2005.

[120] Schroers, J. et al., Gold based bulk metallic glass. *Appl. Phys. Lett.* 87, 061912, 2005.

[121] Ma, H. et al., Doubling the critical size for bulk metallic glass formation in the Mg–Cu–Y ternary system. *J. Mater. Res.* 20, 2252, 2005.

[122] Inoue, A., Zhang, T., and Masumoto, T., Al–La–Ni amorphous alloys with a wide supercooled liquid region. *Mater. Trans. JIM* 30, 965, 1989.

[123] Schroers, J. and Johnson, W.L., Highly processable bulk metallic glass-forming alloys in the Pt–Co–Ni–Cu–P system. *Appl. Phys. Lett.* 84, 3666, 2004.

[124] Inoue, A., Nishiyama, N., and Kimura, H., Preparation and thermal stability of bulk amorphous $Pd_{40}Cu_{30}Ni_{10}P_{20}$ alloy cylinder of 72 mm in diameter. *Mater. Trans. JIM* 38, 179, 1997.

[125] Wert, J.A., Pryds, N., and Zhang, E., Rheological properties of a $Mg_{60}Cu_{30}Y_{10}$ alloy in the supercooled liquid state. *Proceedings of the 22nd Risø International Symposium on Materials Science*, 423, 2001.

[126] Pryds, N.H. et al., Preparation and properties of Mg–Cu–Y bulk amorphous alloys. *Mater. Trans., JIM* 41, 1435, 2000.

[127] Kawamura, Y. et al., High strain-rate superplasticity due to Newtonian viscous flow in $La_{55}Al_{25}Ni_{20}$ metallic glass. *Mater. Trans., JIM* 40, 794, 1999.

[128] Kawamura, Y. et al., Deformation behavior of $Zr_{65}Al_{10}Ni_{10}Cu_{15}$ glassy alloy with wide supercooled liquid region. *Appl. Phys. Lett.* 69, 1208, 1996.

[129] Kündig, A.A., Schweizer, T., Schafler, E., and Löffler, J.F., Metallic glass/polymer composites by co-processing at similar viscosities. *Scripta Mater.* 56, 289, 2007.

[130] Kündig, A.A. et al., Preparation of high aspect ratio surface microstructures out of a Zr-based bulk metallic glass. *Microeletr. Eng.* 67, 405, 2003.
[131] Chokshi, A.H., Mukherjee, A.K., and Langdon, T.G., Superplasticity in advanced materials. *Mater. Sci. Eng. R* 10, 237, 1993.
[132] Kawamura, Y. et al., Full strength compacts by extrusion of glassy metal powder at the supercooled liquid state. *Appl. Phys. Lett.* 67, 2008, 1995.
[133] Saotome, Y., Zhang, T., and Inoue, A. Microforming of MEMS parts with amorphous alloys. *Mat. Res. Soc. Symp. Proc.* 554, 385, 1999.
[134] Zumkley, T. et al., Superplastic forging of ZrTiCuNiBe-bulk glass for shaping of microparts. *Mater. Sci. Forum* 386–388, 541, 2002.
[135] Saotome, Y. et al., The microformability of Pt-based metallic glass and the nanoforming of three-dimensional structures. *Intermetallics* 10, 1241, 2002.
[136] Saotome, Y. et al., Superplastic micro/nano-formability of $La_{60}Al_{20}Ni_{10}Co_5Cu_5$ amorphous alloy in the supercooled liquid state. *Mater. Sci. Eng. A* 304–306, 716, 2001.
[137] Herzer, G., Nanocrystalline soft magnetic materials. *J. Magn. Magn. Mater.* 112, 258, 1992.
[138] Löffler, J.F., Braun, H.B., and Wagner, W., Magnetic correlations in nanostructured ferromagnets. *Phys. Rev. Lett.* 85, 1990, 2000.
[139] Mizoguchi, T., Intrinsic magnetic properties of rapidly solidified alloys (Chap. 16), in *Rapidly Solidified Alloys: Processes, Structure, Properties, Applications*, H.H. Liebermann (Ed.), Dekker Inc., New York, 1993, p. 461.
[140] Hernando, A. and Vázquez, M., Engineering magnetic properties (Chap. 17), in *Rapidly Solidified Alloys: Processes, Structure, Properties, Applications*, H.H. Liebermann (Ed.), Dekker Inc., New York, 1993, p. 553.
[141] Spaepen, F., A microscopic mechanism for steady state inhomogeneous flow in metallic glasses. *Acta Metall.* 25, 407, 1977.
[142] Masumoto, T. and Maddin, R., Mechanical properties of palladium 20 a/o silicon alloy quenched from liquid state. *Acta Metall.* 19, 725, 1971.
[143] Kato, H. et al., Newtonian to non-Newtonian master flow curves of a bulk glass alloy $Pd_{40}Ni_{10}Cu_{30}P_{20}$. *Appl. Phys. Lett.* 73, 3665, 1998.
[144] Lu, J., Ravichandran, G., and Johnson, W.L., Deformation behavior of the $Zr_{41.2}Ti_{13.8}Cu_{12.5}Ni_{10}Be_{22.5}$ bulk metallic glass over a wide range of strain-rates and temperatures. *Acta Mater.* 51, 3429, 2003.
[145] Safarik, D.J., Cady, C.M., and Schwarz, R.B., Shear processes in bulk metallic glasses. *Acta Mater.* 53, 2193, 2005.
[146] Chen, H. S., Kato, H., and Inoue, A., A fictive stress model and nonlinear viscoelastic behaviors in metallic glasses. *Mater. Trans.* 42, 59, 2001.
[147] Argon, A.S., Plastic deformation in metallic glass. *Acta Metall.* 27, 47, 1978.
[148] Lewandowski, J.J. and Greer, A.L., Temperature rise at shear bands in metallic glasses. *Nature Mater.* 5, 15, 2006.
[149] Yang, B. et al., Dynamic evolution of nanoscale shear bands in a bulk metallic glass. *Appl. Phys. Lett.* 86, 141904, 2005.
[150] Dalla Torre, F.H. et al., Negative strain rate sensitivity in bulk metallic glass and its similarities with the dynamic strain aging effect during deformation. *Appl. Phys. Lett.* 89, 091918, 2006.
[151] Wright, W.J., Saha, R., and Nix, W.D., Deformation mechanisms of the $Zr_{40}Ti_{14}Ni_{10}Cu_{12}Be_{24}$ bulk metallic glass. *Mater. Trans., JIM* 42, 642, 2001.
[152] Bowman, K., *Mechanical Behaviour of Materials*, John Wiley & Sons, Inc., Hoboken, USA, 2004.
[153] Lewandowski, J.J., Wang, W.H. and Greer, A.L., Intrinsic plasticity or brittleness of metallic glasses. *Phil. Mag. Lett.* 85, 77, 2005.
[154] Lewandowski, J.J., Shazly, M., and Nouri, A.S., Intrinsic and extrinsic toughening of metallic glasses. *Scripta Mater.* 54, 337, 2006.

[155] Callister, W.D., *Materials Science and Engineering: An Introduction.* John Wiley & Sons, Inc., New York, 1994, p. 194.
[156] Cockeram, B.V., The fracture toughness and toughening mechanisms of nickel-base wear materials. *Metall. Mater. Trans. A* 33, 33, 2002.
[157] Wang, R.J. et al., Responses of glassy structure and properties to pressure and devitrification. *Appl. Phys. Lett.* 83, 2814, 2003.
[158] Xi, X.K. et al., Fracture of brittle metallic glasses: Brittleness or plasticity. *Phys. Rev. Lett.* 94, 125510, 2005.
[159] Wesseling, P. et al., Preliminary assessment of flow, notch toughness, and high temperature behavior of $Cu_{60}Zr_{20}Hf_{10}Ti_{10}$ bulk metallic glass. *Scripta Mater.* 51, 151, 2004.
[160] Saida, J. et al., Crystallization and grain growth behavior of $Zr_{65}Cu_{27.5}Al_{7.5}$ metallic glass. *Mater. Sci. Eng.* A 304, 338, 2001.
[161] Wang, W.H., Dong, C., and Shek, C.H., Bulk metallic glasses. *Mater. Sci. Eng.* R 44, 45, 2004.
[162] Lowhaphandu, P. and Lewandowski, J.J., Fracture toughness and notched toughness of bulk amorphous alloy: Zr–Ti–Ni–Cu–Be. *Scripta Mater.* 38, 1881, 1998.
[163] Gilbert, C.J., Schroeder, V., and Ritchie, R.O., Mechanisms for fracture and fatigue-crack propagation in a bulk metallic glass. *Metal. Mater. Trans. A.* 30, 1739, 1999.
[164] Flores, K.M., Johnson, W.L., and Dauskardt, R.H., Fracture and fatigue behavior of a Zr–Ti–Nb ductile phase reinforced bulk metallic glass matrix composite. *Scripta Mater.* 49, 1181, 2003.
[165] Wetzig, K. et al., The relaxation behavior of strength and fracture-toughness of amorphous metal–metalloid alloys. *Cryst. Res. Technol.* 18, 1181, 1983.
[166] Davis, L.A., Fracture of Ni–Fe based metallic glasses. *J. Mater. Sci.* 10, 1557 , 1975.
[167] Schroers, J. and Johnson, W.L., Ductile bulk metallic glass. *Phys. Rev. Lett.* 93, 255506, 2004.
[168] Nagendra, N. et al., Effect of crystallinity on the impact toughness of a La-based bulk metallic glass. *Acta Mater.* 48, 2603, 2000.
[169] Pugh, S.F., Relations between the elastic moduli and the plastic properties of polycrystalline pure metals. *Phil. Mag.* 45, 823, 1954.
[170] Kelly, A., Tyson, W.R., and Cottrell, A.H., Ductile and brittle crystals. *Phil. Mag.* 15, 567, 1967.
[171] Rice, J.R. and Thomson, R., Ductile versus brittle behavior of crystals. *Phil. Mag.* 29, 73, 1974.
[172] Johnson, W.L. and Samwer, K., A universal criterion for plastic yielding of metallic glasses with a $(T/T_g)^{2/3}$ temperature dependence. *Phys. Rev. Lett.* 95, 195501, 2005.
[173] Van den Beukel, A. and Radelaar, S., On the kinetics of structural relaxation in metallic glasses. *Acta Metall.* 31, 419, 1983.
[174] Van den Beukel, A., Analysis of structural relaxation data in metallic glasses in terms of different models. *Acta Metal. Mater.* 39, 2709, 1991.
[175] Kato, H. et al., Newtonian to non-Newtonian master flow curves of a bulk glass alloy $Pd_{40}Ni_{10}Cu_{30}P_{20}$. *Appl. Phys. Lett.* 73, 3665, 1998.
[176] Kawamura, Y. and Inoue, A., Newtonian viscosity of supercooled liquid in a $Pd_{40}Ni_{40}P_{20}$ metallic glass. *Appl. Phys. Lett.* 77, 1114, 2000.
[177] Wang, G. et al., Tensile fracture characteristics and deformation of a Zr-based bulk metallic glass at high temperatures. *Intermetallics* 13, 642, 2005.
[178] Hays, C.C., Kim, C.P., and Johnson, W.L., Microstructure controlled shear band pattern formation and enhanced plasticity of bulk metallic glasses containing in situ formed ductile phase dendrite dispersions. *Phys. Rev. Lett.* 84, 2901, 2000.
[179] Lee, M.L., Li, Y., and Schuh, C.A., Effect of a controlled volume fraction of dendritic phases on tensile and compressive ductility in La-based metallic glass matrix composites. *Acta Mater.* 52, 4121, 2004.
[180] Kühn, U. et al., ZrNbCuNiAl bulk metallic glass matrix composites containing dendritic bcc phase precipitates. *Appl. Phys. Lett.* 80, 2478, 2002.
[181] He, G. et al., Novel Ti-base nanostructure–dendrite composite with enhanced plasticity. *Nature Mater.* 2, 33, 2003.

[182] Xu, Y. et al., Mg-based bulk metallic glass composites with plasticity and gigapascal strength. *Acta Mater.* 53, 1857, 2005.
[183] Das, J. et al., Work-hardenable ductile bulk metallic glass. *Phys. Rev. Lett.* 94, 205501, 2005.
[184] Choi-Yim, H. and Johnson, W.L., Bulk metallic glass matrix composites. *Appl. Phys. Lett.* 71, 3808, 1997.
[185] Choi-Yim, H. et al., Synthesis and characterization of particulate reinforced $Zr_{57}Nb_5Al_{10}Cu_{15.4}Ni_{12.6}$ bulk metallic glass composites. *Acta Mater.* 47, 2455, 1999.
[186] Siegrist, M.E. and Löffler, J.F., Bulk metallic glass-graphite composites. *Scripta Mater.* (submitted).
[187] Schroers, J., Veazey, C., and Johnson, W.L., Amorphous metallic foam. *Appl. Phys. Lett.* 82, 370, 2003.
[188] Wada, T., Greer, A.L., and Inoue, A., Enhancement of room-temperature plasticity in a bulk metallic glass by finely dispersed porosity. *Appl. Phys. Lett.* 86, 251907, 2005.
[189] Brothers, A.H. and Dunand, D.C., Plasticity and damage in cellular amorphous metals. *Acta Mater.* 53, 4427, 2005.
[190] Ashby, M.F. et al., *Metal Foams: A Design Guide.* Butterworth Heinemann, Woburn, 2000.
[191] Brothers, A.H. and Dunand, D.C., Processing and structure of open-celled amorphous metal foams. *Scripta Mater.* 52, 335, 2005.
[192] Kündig, A.A. et al., In situ formed two-phase metallic glass with surface fractal microstructure. *Acta Mater.* 52, 2441, 2004.
[193] Park, B.J. et al., In situ formation of two amorphous phases by liquid phase separation in Y–Ti–Al–Co alloy. *Appl. Phys. Lett.* 85, 6353, 2004.
[194] Mattern, N. et al., Microstructure and thermal behavior of two-phase amorphous Ni–Nb–Y alloy. *Scripta Mater.* 53, 271, 2005.
[195] Oh, J.C. et al., Phase separation in $Cu_{43}Zr_{43}Al_7Ag_7$ bulk metallic glass, *Scripta Mater.* 53, 165, 2005.
[196] www.metglas.com (Metglas® Magnetic Materials).
[197] Andersen III, P.M., Bretts, G.R., and Kearney, J.E., Surveillance system having magnetomechanical marker. U.S. Patent 4,510,489, 1985.
[198] Mastrogiacomo, G., Kradolfer, J., and Löffler, J.F., Development of magnetic Fe-based metallic glasses without metalloids. *J. Appl. Phys.*, 99, 023908, 2006.
[199] http://www.liquidmetal.com (Liquidmetal®Technologies).
[200] www.ocrwm.doe.gov/osti/pdf/43757.pdf (Advanced Technologies, FY2004 Project: High-performance corrosion-resistant coatings, U.S. Department of Energy, Office of civilian radioactive waste management).
[201] Tschan, R. et al., Semihydrogenation of a propargylic alcohol over highly active amorphous $Pd_{81}Si_{19}$ in "supercritical" carbon dioxide. *Appl. Catal. A* 223, 173, 2002.
[202] Ma, C., Nishiyama, N., and Inoue, A., Fabrication and characterization of Coriolis mass flowmeter made from Ti-based glassy tubes. *Mater. Sci. Eng. A* 407, 201, 2005.
[203] Inoue, A., Bulk glassy and nonequilibrium crystalline alloys by stabilization of supercooled liquid: fabrication, functional properties and applications (Part 2). *Proc. Jpn. Acad. Ser. B* 81, 172, 2005.
[204] Ishida, M. et al., Fillability and imprintability of high-strength Ni-based bulk metallic glass prepared by the precision die-casting technique. *Mater. Trans., JIM* 44, 1239, 2004.
[205] Sharma, P. et al., Nanoscale patterning of Zr–Al–Cu–Ni metallic glass thin films deposited by magnetron sputtering. *J. Nanosci. Nanotechnol.* 5, 416, 2005.
[206] Jin, K. and Löffler, J.F., Bulk metallic glass formation in Zr–Cu–Fe–Al alloys. *Appl. Phys. Lett.* 86, 241909, 2005.
[207] Buzzi, S. et al., Cytotoxicity of Zr-based bulk metallic glasses. *Intermetallics* 14, 729, 2006.